Further examination of the thermodynamic modification of the inflow layer of tropical cyclones by vertical wind shear

M. Riemer[1], M. T. Montgomery[2,3], and M. E. Nicholls[4]

[1]Institut für Physik der Atmosphäre, Johannes Gutenberg-Universität, Mainz, Germany
[2]Department of Meteorology, Naval Postgraduate School, Monterey, California, USA
[3]NOAA's Hurricane Research Division, Miami, Florida, USA
[4]University of Colorado, Cooperative Institute for Research in Environmental Sciences, Boulder, CO, USA

Correspondence to: Michael Riemer
(mriemer@uni-mainz.de)

Abstract. Recent work has developed a new framework for the impact of vertical wind shear on the intensity evolution of tropical cyclones. A focus of this framework is on the frustration of the tropical cyclone's power machine by shear-induced, persistent downdrafts that flush relatively cool and dry (lower equivalent potential temperature, θ_e) air into the storm's inflow layer. These previous results have been based on idealised numerical experiments for which we have deliberately chosen a simple set of physical parameterisations. Before efforts are undertaken to test the proposed framework with real atmospheric data, we here survey and diagnose five additional numerical experiments with some modifications of the experimental setup to assess the robustness of our previous results. The modifications comprise the values of the exchange coefficients of surface heat and momentum fluxes, the inclusion of experiments with ice microphysics, and the consideration of weaker, but still mature tropical cyclones.

In all experiments, the depression of the inflow layer θ_e values is significant and all tropical cyclones exhibit the same general structural changes when interacting with the imposed vertical wind shear. Tropical cyclones with a higher downdraft activity exhibit a more pronounced depression of inflow layer θ_e *outside* of the eyewall in our experiments. The magnitude of the θ_e depression *underneath* the eyewall early after shear is imposed in our experiments correlates well with the magnitude of the ensuing weakening of the respective tropical cyclone. Based on the evidence presented, it is concluded that the newly proposed framework is a robust description of intensity modification in our suite of experiments.

Report Documentation Page		Form Approved OMB No. 0704-0188

1. REPORT DATE **OCT 2011**	2. REPORT TYPE	3. DATES COVERED **00-00-2011 to 00-00-2011**
4. TITLE AND SUBTITLE **Further examination of the thermodynamic modification of the inflow layer of tropical cyclones by vertical wind shear**		5a. CONTRACT NUMBER
		5b. GRANT NUMBER
		5c. PROGRAM ELEMENT NUMBER
6. AUTHOR(S)		5d. PROJECT NUMBER
		5e. TASK NUMBER
		5f. WORK UNIT NUMBER
7. PERFORMING ORGANIZATION NAME(S) AND ADDRESS(ES) **Naval Postgraduate School,Department of Meteorology,Monterey,CA,93943**		8. PERFORMING ORGANIZATION REPORT NUMBER
9. SPONSORING/MONITORING AGENCY NAME(S) AND ADDRESS(ES)		10. SPONSOR/MONITOR'S ACRONYM(S)
		11. SPONSOR/MONITOR'S REPORT NUMBER(S)

12. DISTRIBUTION/AVAILABILITY STATEMENT **Approved for public release; distribution unlimited**

13. SUPPLEMENTARY NOTES

14. ABSTRACT

Recent work has developed a new framework for the impact of vertical wind shear on the intensity evolution of tropical cyclones. A focus of this framework is on the frustration of the tropical cyclone?s power machine by shear-induced, persistent downdrafts that flush relatively cool and dry (lower equivalent potential temperature, e) air into the storm?s inflow layer. These previous results 5 have been based on idealised numerical experiments for which we have deliberately chosen a simple set of physical parameterisations. Before efforts are undertaken to test the proposed framework with real atmospheric data, we here survey and diagnose five additional numerical experiments with some modifications of the experimental setup to assess the robustness of our previous results. The modifications comprise the values of the exchange coefficients of surface heat and momentum fluxes 10 the inclusion of experiments with ice microphysics, and the consideration of weaker, but still mature tropical cyclones. In all experiments, the depression of the inflow layer e values is significant and all tropical cyclones exhibit the same general structural changes when interacting with the imposed vertical wind shear. Tropical cyclones with a higher downdraft activity exhibit a more pronounced depression of 15 inflow layer e outside of the eyewall in our experiments. The magnitude of the e depression underneath the eyewall early after shear is imposed in our experiments correlates well with the magnitude of the ensuing weakening of the respective tropical cyclone. Based on the evidence presented, it is concluded that the newly proposed framework is a robust description of intensity modification in our suite of experiments.

15. SUBJECT TERMS					

16. SECURITY CLASSIFICATION OF:			17. LIMITATION OF ABSTRACT	18. NUMBER OF PAGES	19a. NAME OF RESPONSIBLE PERSON
a. REPORT **unclassified**	b. ABSTRACT **unclassified**	c. THIS PAGE **unclassified**	**Same as Report (SAR)**	**37**	

1 Introduction

1.1 A new framework for intensity modification of tropical cyclones in vertical wind shear

The intensity evolution of tropical cyclones (TCs) embedded in an environmental flow with vertical wind shear poses an important forecast problem. To date, the physical processes that govern this intensity evolution are not well understood. In a recent publication (Riemer et al., 2010, referred to as RMN10 hereafter) a new framework for the intensity modification of TCs in vertical wind shear was proposed. While previous hypotheses have focused almost exclusively on processes above the boundary layer, RMN10 showed that vertical wind shear has a significant impact on the thermodynamic properties of the TC's inflow layer[1]. Strong and persistent, shear-induced downdrafts flush the inflow layer with low moist-entropy (or equivalent potential temperature, θ_e) air - "anti-fuel" for the TC power machine. The replenishment of this air by surface heat fluxes is not complete while the air spirals towards the storm centre leading to a reduction of θ_e values within the inner-core updrafts in the *azimuthal mean*. When viewed from the simplified perspective of an idealised Carnot-cycle a decrease in the potential intensity of the TC can be expected (Tang and Emanuel, 2010).

The downdrafts that flush the inflow layer with low-θ_e air are associated with a quasi-stationary, azimuthal wave-number 1, convective asymmetry *outside* of the eyewall. This convective asymmetry is reminiscent of the 'stationary band complex' (Willoughby et al., 1984) and for this reason will be referred to as the SBC hereafter. The SBC and the associated downdraft pattern extends outwards to approximately 150 km – 180 km. On account of the swirling winds, the updrafts within the SBC rise along a helical path. A simple kinematic model (Riemer and Montgomery, 2011) suggests that, at low levels above the inflow layer, environmental low-θ_e air approaches the storm closely underneath the helical updrafts in the downshear and downshear-left quadrants. Evaporative cooling of precipitation falling out of the SBC, and into this unsaturated air, most likely drives the strong and persistent, vortex-scale downdrafts that cool and dry the TC's inflow layer.

In RMN10, evidence was presented that the formation of the SBC is connected to the tilt[2] of the TC vortex. When subject to vertical wind shear, the tilt evolution of the TC vortex was shown to be governed to zero order by asymmetric-balance dynamics. Vortex tilt can thus be described in terms of a standing vortex-Rossby-wave (VRW) pattern with azimuthal and vertical wave-number 1 structure. Even though the tilt of the inner core is only 10 km–20 km, the VRW pattern associated with the tilt of the outer vortex extends outwards to radii of 150 km–200 km (Fig. 15a in RMN10)[3]. After vertical

---

[1]In the current study, the term 'inflow layer' will refer to the layer of strong inflow associated with surface friction in the lowest 1 km - 1.5 km where the departure from gradient wind balance in the radial direction is generally a maximum (e.g., Bui et al. (2009), their Figs. 5 and 6 and accompanying discussion).

[2]In RMN10, the tilt is defined as the vector difference between the location of the vorticity centroids at 10 km and 1 km height.

[3]A considerable tilt of the outer parts of TC-like vortices with small tilt of the inner core has been noted previously by other authors also (see e.g. Fig. 6a in Jones (1995), Fig. 10 in Reasor et al. (2004)).

50   wind shear is suddenly imposed, the TC settles quickly (approx. within 3 h) into a quasi-equilibrium

tilt direction that is to the downshear-left. Thus, the positive vorticity anomaly associated with the

standing wave-number 1 VRW pattern is found downshear-left at upper levels and downshear-right

at low levels. Frictional convergence associated with this positive low-level vorticity anomaly then

provides forcing for the asymmetric convection within the SBC. The foregoing results suggest an

55   important connection between the asymmetric-balance dynamics governing the tilt evolution of the

vortex subject to vertical shear and the thermodynamic impact on the inflow layer.

The findings of RMN10 were derived from idealised numerical experiments following the setup

of Bender (1997) and Frank and Ritchie (2001). In this experimental setup, a uni-directional vertical

wind shear profile is imposed suddenly on a mature model TC. In an attempt to minimise complex-

60   ity and to understand the fundamental processes, RMN10 deliberately chose a simple set of model

parameterisations. As is the nature of results derived from such an idealised approach, uncertainties

exist whether the newly proposed pathway operates in the real atmosphere. Although some prelimi-

nary observational support was offered in RMN10 a more comprehensive test of the new hypothesis

with atmospheric data awaits future studies. Before undertaking such efforts we here survey and

65   diagnose five additional numerical experiments with some modifications of the experimental setup

to assess the robustness of RMN10's results.

1.2   Summary of numerical experiments

The numerical experiments in RMN10 employed a microphysics scheme that considers "warm

cloud" processes associated with the collision-coalescence process only (hereafter termed "warm

70   rain"). The current study considers experiments with ice microphysics also. Adding ice processes in-

troduces the latent heat of fusion/ sublimation, new classes of hydrometeors with various fall speeds,

and additional pathways to form precipitation. Details of the employed ice microphysic scheme are

given in section 2.2. Arguably, the most significant of the above processes is the additional conver-

sion of latent heat associated with the freezing and melting of ice. Ice microphysics produce stronger

75   updrafts than a warm-rain scheme due to the additional latent heat release associated with freezing.

In addition, the inclusion of precipitation in the form of ice may significantly enhance the formation

and intensity of downdrafts (Srivastava, 1987).

Previous studies have shown that the inclusion of ice microphysics in numerical models may

alter the radial profile of the swirling winds of TCs as compared to a warm-rain experiment (e.g.

80   Fovell et al., 2009). In general, it is not well understood how these differences arise. Fovell et al.

have proposed a mechanism that is based on the sedimentation of ice particles from the outflow

anvil, the subsequent sublimation of these ice particles, and radiative feedback. In our suite

of experiments, however, radiative processes are neglected. Nevertheless, potentially significant

differences in the TC-vortex structure between the warm-rain and the ice microphysic experiments

85   do arise, indicating that the mechanism suggested by Fovell et al. is not of primary importance. The

3

potentially important differences in the TC-vortex structure and their implication for the interaction with vertical wind shear will be discussed in some detail in section 3.1.

Recent studies have highlighted the importance of the representation of the planetary boundary layer in numerical models for vortex intensification and structure changes of simulated storms (Braun and Tao, 2000; Smith and Thomsen, 2010; Montgomery et al., 2010; Smith et al., 2011). The exchange coefficients for enthalpy, C_K, and momentum, C_D, play a most prominent role. They govern the energy extraction from the ocean surface and the dissipation of kinetic energy in the frictional boundary layer, respectively. In the framework of RMN10, the values of C_K and C_D can be expected to play an important role in the replenishment of the depressed boundary layer θ_e air while spiralling towards the inner-core updrafts. The replenishment rate is proportional to C_K[4]. The strength of the inflow within the frictional boundary layer is determined in part by C_D. Smaller values of C_D may lead to less radial inflow and thus to an *increase* of the replenishment time. Assuming that C_K is not changed, the replenishment of depressed inflow layer θ_e values is then *more complete* than for larger values of C_D. Based on these considerations, one would expect that the shear-induced flushing of the inflow layer with low-θ_e air has a more pronounced impact on TC intensity for smaller values of C_K and larger values of C_D. The interpretation of the importance of C_K and C_D in an axisymmetric theory for a TC in vertical wind shear by Tang and Emanuel (2010) is consistent with the foregoing considerations.

Considerable uncertainties exist about the values of C_K and C_D at the high wind speeds occurring in TCs. Deacon's formula for C_D was employed in RMN10 and the ratio of C_K/C_D was set to unity. Recent results derived from observational data (Black et al., 2007; Zhang et al., 2008) strongly indicate that Deacon's formula overestimates C_D at high wind speeds and that C_K/C_D is considerably less than unity. The observational data exhibit considerable scatter and are limited to wind speeds of marginal hurricane strength[5]. To address the likely overestimation of C_K and C_K/C_D in RMN10, we employ in this study values of C_K and C_K/C_D that are consistent with, but rather on the lower end of the range of values observed by Black et al. and Zhang et al.. Further details are provided in section 2.3.

The TCs considered in RMN10 were intense and rapidly intensifying at the time when the vertical wind shear profile was imposed. In the current study we will consider, inter alia, weaker, but still mature TCs. Finally, our additional experiments now exhibit various rates of intensification just before vertical wind shear is imposed. We did not, however, find a sensitivity of the subsequent TC evolution in vertical shear on this preceding intensification rate in our experiments. Thus, the various rates of intensification just before vertical wind shear is imposed will not be considered hereafter.

The next section provides an overview of the numerical model employed and the additional experiments performed, an expanded description of the ice microphysics scheme, and the values for

---

[4]The replenishment rate is proportional to the air-sea thermodynamic disequilibrium also.

[5]Some significant strides towards determining these coefficients at major hurricane wind conditions have been made recently by Bell (2010) as part of his Ph.D. dissertation.

4

the surface exchange coefficients. In section 3 we compare the evolution of the quintessential ingredients of RMN10's newly proposed framework in the different numerical experiments. One experiment with ice microphysics is examined in further detail in section 4, including an estimate of the spindown time-scale of the simulated TC-vortex based on simple axisymmetric theory. Section 5 contains our conclusions.

2 Model setup and additional experiments

2.1 A brief model description

For the numerical experiments we employ the Regional Atmospheric Modeling System (RAMS), developed at Colorado State University (Pielke and Coauthors, 1992; Cotton and Coauthors, 2003). The RAMS is a three-dimensional, non-hydrostatic numerical modeling system comprising time-dependent equations for velocity, non-dimensional pressure perturbation, ice-liquid water potential temperature (Tripoli and Cotton, 1981), and mixing ratios of total water and hydrometeors.

A standard first-order turbulence scheme developed by Smagorinsky (1963) is used for sub-grid-scale mixing, with modifications by Lilly (1962) and Hill (1974) that enhance diffusion in unstable conditions and reduce diffusion in stable conditions. For simplicity, radiative processes are neglected. The bulk aerodynamic formulas are used to calculate momentum and sensible and latent heat fluxes from the sea surface. The values of the exchange coefficients are given in subsection 2.3. We either employ a warm-rain microphysics scheme based on the scheme of Kessler (1969) or the RAMS standard ice microphysics scheme (subsection 2.2). A comprehensive description of RAMS, the surface interaction parameterisation, and the warm-rain scheme is given in RMN10.

2.2 Ice microphysics in RAMS

The RAMS ice microphysics scheme has eight water categories: vapour, cloud droplets, rain, pristine ice, snow, aggregates, graupel and hail (Walko et al., 1995; Meyers et al., 1997). The liquid phase categories, cloud droplets and rain, may be supercooled. Pristine ice, snow and aggregates are assumed to be completely frozen, whereas graupel and hail are mixed phase categories, capable of consisting of ice only, or a mixture of ice and liquid. All hydrometeor categories except cloud droplets are assumed large enough to fall. Cloud droplets and pristine ice are the only categories to nucleate from vapour. All other categories form from existing hydrometeors, but once formed may also grow by vapour deposition. Pristine ice crystals form from heterogeneous nucleation, homogeneous nucleation, and secondary production that involves splintering of riming crystals. The snow category is defined in RAMS as relatively large ice crystals, which have grown from the pristine ice category due to vapour deposition and may continue to grow by riming. Aggregates are defined as ice particles that have formed by collision and coalescence of pristine ice, snow and/or aggregates. Snow and aggregates retain their identity with moderate amounts of riming, but convert to graupel

5

155   if the amount of riming is large. In addition to forming by heavy riming graupel can also form by
partial melting of snow or aggregates. Graupel is allowed to carry up to half its mass in liquid. If
the percentage becomes larger, by either melting, riming or collection by rain, a graupel particle is
re-categorised as hail. Hail is formed by freezing of rain drops or by riming or partial melting of
graupel. Hail is allowed to be a large fraction liquid and converts to rain when completely liquid.

160   The hydrometeor size distribution in RAMS is represented by a generalised Gamma function. A
user specified shape parameter controls the width of the distribution. Also, a scaling diameter is
often specified for a one-moment scheme that is related to the mean diameter of the distribution,
with the particular relation depending on the chosen spectral parameters. For this study a one-
moment scheme is employed for all categories except cloud droplets and pristine ice. A scaling
165   diameter is specified and the number concentration is diagnosed using the predicted mixing ratio of
the hydrometeor scheme.

A heat budget equation is formulated for rain, graupel, and hail hydrometeors. This allows the
temperature of a hydrometeor to differ from that of the surrounding ambient air temperature due to
latent heat release or absorption in the hydrometeor, and sensible heating by collisions with other
170   hydrometeors. The temperature of a hydrometeor often differs substantially from that of the air,
which can significantly influence the rates of heat and vapour diffusion, as well as the amount of
sensible heat transfer that occurs in coalescence of hydrometeors. Collision and coalescence of
hydrometeors is governed by the stochastic equation derived by Verlinde et al. (1990).

Gravitational settling of hydrometeors causes them to fall relative to air. Terminal velocities in-
175   crease as a power of the droplet diameter, and are based on empirical data. Pristine ice has very small
fall speeds. Snow crystals fall faster than pristine ice, but still relatively slowly. Aggregates are large
crystals that have moderate fall speeds. Graupel and hail have high fall speeds. Sedimentation in
RAMS uses a Lagrangian scheme to transport the mixing ratio from any given grid cell to a lower
height in the vertical column, so that a proportion is transferred to the lower adjacent grid cell.

180   ## 2.3 Modification of surface exchange coefficients

Deacon's formula for the dependence of the drag exchange coefficient C_D on wind speed is given
by

$$C_D = 1.1 \times 10^{-3} + 4 \times 10^{-5} |V|^1, \tag{1}$$

with $|V|^1$ being the wind speed in ms^{-1} at the lowest model level (here: 49 m). In RMN10 we used
185   Deacon's formula and $C_K = C_D$. For reference, this formula furnishes values of the exchange coef-
ficients of 1.5×10^{-3}, 2.1×10^{-3}, and 3.1×10^{-3} for 10 ms^{-1}, 25 ms^{-1}, and 50 ms^{-1}, respectively.

Zhang et al. (2008) found that 'The exchange coefficient of enthalpy flux shows no significant
dependence on wind speed up to hurricane force with a value of 1.16×10^{-3}.' and that 'The average

6

ratio of the C_K/C_D values is 0.63, ...'. We therefore use these values and set

$$C_K = 1.16 \times 10^{-3} = \text{constant} \tag{2}$$

and

$$C_K/C_D = 0.63. \tag{3}$$

Experiments that employ these values are referred to as CBLAST below. Note that Deacon's formula and $C_K/C_D = 1$ furnishes values of C_K and C_D that, for $|V|^1 = 50$ ms^{-1}, are approx. 2.7 and 4.2 times higher, respectively, than the corresponding CBLAST values.

2.4 Summary of experiments

A summary of the experiments examined in this study is given in table 1. We refer to experiments that employ warm rain and Deacon's formula for the exchange coefficients (with $C_K/C_D = 1$) as RMN. The CBLAST experiments employ warm rain also. Experiments that include ice microphysics are referred to as ICE. ICE experiments use Deacon's formula with $C_K/C_D = 1$.

The shear profile employed in this study has a cosine structure in the vertical with zero winds at the surface and maximum easterly winds at 12 km and above. We will follow the convention of the TC community to define vertical wind shear as the vector difference between the winds at upper and lower levels. Here, we use the vector difference between 12 km and the surface. The shear magnitude is thus given in ms^{-1}. Unless otherwise noted, we will consider TCs in vertical wind shear with a magnitude of 15 ms^{-1}. The shear profile is imposed at a high intensity[6] of 68 ms^{-1}, after the TCs have spun up in quiescent environment. These experiments are referred to as RMN$_{68}$, CBLAST$_{68}$, and ICE$_{68}$, respectively. The intensity at the time when shear is imposed will be referred to as "initial intensity" below. Experiment RMN$_{68}$ is the 15mps case of RMN10 and constitutes our reference experiment.

We have performed experiments with a weaker initial intensity of 54 ms^{-1} also, referred to as RMN$_{54}$ and CBLAST$_{54}$. Furthermore, an ICE experiment has been performed with 10 ms^{-1} vertical shear ($_{10}$ICE$_{68}$) which will be compared briefly to the 10mps case of RMN10 (here: $_{10}$RMN$_{68}$).

3 Assessing the robustness of the new framework

We shall focus on the key features of RMN10's new framework for intensity modification in vertical wind shear: the vortex tilt, the occurrence and location of the SBC, the flushing of the inflow layer with low-θ_e air, the ensuing depression of inflow layer θ_e, and the associated weakening of the TC. The general characteristics of these key feature will be found to be consistent in all experiments.

---

[6]The storm intensity metric in this study, as well as in RMN10, is the maximum azimuthally averaged tangential wind speed at 1 km height.

7

As can be expected, differences arise in the specific characteristics of these key features. For some
of these differences it is very difficult to establish the causal link to the changes in the experimental
setup. Most prominently, differences between the evolution of the TCs in RMN_{68} and ICE_{68} are
partly due to the enhancement of downdrafts by ice microphysics (Sec. 3.7) but very likely also
due to changes in the radial profile of the swirling winds at the time when vertical wind shear is
imposed. Disentangling the individual contributions requires a more complete understanding of the
processes at work, and extended numerical experimentation and diagnostic analyses, preferably in an
ensemble-based framework. A more comprehensive examination of such differences is thus deferred
to future research.

3.1 Importance of the radial profile of the swirling winds

3.1.1 Impact on the resiliency of TC-like vortices

It is generally believed that the presence of vertical wind shear increases the interaction of a TC with
dry environmental air (Riemer and Montgomery, 2011, and references therein). Based on a simple
kinematic model, Riemer and Montgomery (2011) argue that a TC with a broad radial profile of the
swirling winds should have a stronger ability to isolate itself from the detrimental interaction with
dry environmental air than a smaller-scale TC. Furthermore, the radial profile of the swirling winds
has a profound impact on the *dynamic* resiliency of TC-like vortices, i.e. the ability to maintain
vertical coherence in the presence of differential advection by the vertical shear flow (e.g. Jones,
1995; Reasor et al., 2004). These studies investigated the resiliency of initially barotropic, dry
vortices and are reviewed briefly below.

Jones (1995) examined vortex evolution in terms of the formation and subsequent interaction of
potential vorticity (PV) anomalies. PV anomalies were defined as deviations from the azimuthal
mean. Due to the differential advection by the vertical shear flow, PV anomalies representing the
tilt of the vortex form at lower and upper levels. These anomalies mutually interact through the
vertical penetration of their "induced" quasi-horizontal circulations, causing the vortex to precess.
This precession helps the vortex to counteract the differential advection by the vertical wind shear.
In general, the vertical interaction of PV anomalies depends on the Rossby penetration depth. The
penetration depth increases with the strength of the background rotation and with the horizontal scale
of the interacting anomalies. Jones noted that it is not entirely clear how to quantify the penetration
depth for a tilted TC-like vortex but concluded that intense and broad vortices are more resilient than
their weaker, smaller-scale counterparts.

Reasor et al. (2004) re-visited the problem of vortex resiliency and re-alignment using VRWs con-
cepts and models. Their results are in qualitative agreements with Jones's finding that vortex (and
environment) parameters that increase the penetration depth improve the resistence of a vortex to
tilting by an imposed vertical shear flow. In addition, Reasor et al. demonstrated that vortex preces-

sion is not the only element in the resiliency of TC-like vortices. An inviscid damping mechanism of the vortex-tilt mode exists, associated with PV mixing at the critical radius of the near-discrete VRW that represents the vortex tilt. The critical radius is typically located in the "skirt" region of the vortex, i.e. in the region of small PV values outside of the high-PV values in the inner core (approx. outside 50 km - 70 km in Fig. 1(a)). The inviscid damping mechanism depends on the radial gradient of the skirt PV at the critical radius (Schecter and Montgomery, 2003). Inviscid damping, and thus re-alignment of the vortex, occurs when the radial PV gradient in this region is negative. The damping rate increases with the magnitude of the gradient. For a positive skirt-PV gradient a tilt instability may occur. Reasor et al. 's results clearly demonstrate that vortex resiliency may crucially depend on the radial profile of the swirling winds.

The radial profile of the swirling winds has been confirmed to play a role in the intensity evolution of vertically sheared TCs in idealised, moist numerical experiments (Wong and Chan, 2004). In these experiments the weakening of smaller-scale TCs is found to be more pronounced than that of their broader-scale counterparts. Wong and Chan based their interpretation of this difference in the intensity evolution on the results of Jones (1995) derived from dry TC-like vortices. To us, however, it is not clear what the underlying processes are that govern the intensity evolution in Wong and Chan's experiments. In particular, the role of *moist* processes and/or the associated secondary circulation remain unclear.

In the real atmosphere, an indication of a higher susceptibility of smaller-scale TCs to vertical shear has been found by DeMaria (1996) based on a regression analysis.

3.1.2 Diagnosed radial vortex structure in our experiments

Because the radial profile of the swirling winds may play a prominent role in the evolution of TCs in vertical wind shear, we begin the examination of our experiments with the comparison of the vortex structure at the time when vertical wind shear is imposed. The radial, azimuthal mean profiles of the swirling winds at this time are illustrated in Fig. 1. In $CBLAST_{68}$, the radius of maximum winds (RMW) is found at 40 km (Fig. 1(a)). The vorticity maximum is 35×10^{-4} s^{-1} at a radius of 20 km. This vortex structure is very similar as in RMN_{68} (shown in Fig. 4 in RMN10)[7]. For the weaker TC in $CBLAST_{54}$, the vorticity structure outside a radius of 35 km is almost identical to $CBLAST_{68}$. Inside this radius, vorticity is virtually constant with a value of approx. 20×10^{-4} s^{-1}. The corresponding RMW is found at 48 km. The initial radial structure of the TC in RMN_{54} is very similar (not shown).

The vorticity structure of the TC in ICE_{68} exhibits some notable differences as compared to the warm-rain experiments $CBLAST_{68}$ and RMN_{68}. The vorticity maximum is found inside a radius of 10 km with values of 55×10^{-4} s^{-1}, i.e. approx. 60 % higher than in $CBLAST_{68}$. Radially outside

---

[7]A potential impact of barotropic instability associated with the reversal of the radial vorticity gradient in the inner core on the intensity evolution of the sheared TCs in our experiments is arguably negligible (see Sec. 3.1 in RMN10).

of this maximum, the high vorticity values decrease rapidly. Corresponding to the smaller radius of maximum vorticity, the RMW is smaller (located at 30 km) than in $CBLAST_{68}$ and RMN_{68} also.

As discussed above, the resiliency of the TC vortex may crucially depend on the gradient of (potential) vorticity at the critical radius of the (near-discrete) VRW mode that represents the vortex tilt. The critical radius is found where the azimuthal propagation of this VRW, i.e. the vortex precession, equals the speed of the swirling winds. The precession rate, and thus the critical radius, in our experiments is difficult to determine. After the vortices have re-aligned, a short precession period of 2 h - 3 h is indicated in all experiments (see Fig. 4 below[8]). Using the values of the axisymmetric swirling winds at 1 km, as depicted in Fig. 1(a), our rough estimate of the critical radius is then 50 km - 90 km.

In ICE, the vorticity gradient is near-zero between 50 km and 65 km while in $CBLAST_{68}$ and RMN_{54} the gradient is negative and of large magnitude (Fig. 1(b)). Between 65 km and 100 km the radial vorticity profiles are broadly similar. At larger radii (not shown) the average vorticity gradient is *positive* in RMN_{54} (between 120 km and 200 km) and ICE (between 150 km - 200 km). In CBLAST, in contrast, vorticity decreases monotonically out to 200 km radius. It is questionable, however, whether these differences at a radius considerably larger than our estimate for the critical radius play a role for the TC-vortex evolution in our experiments.

From the discussion in this subsection it is clear that differences in the evolution of the TCs when interacting with the vertical shear flow in the various experiments potentially arise due to differences in the radial vorticity profiles *before* shear is imposed. The weaker vortices in RMN_{54} and $CBLAST_{54}$, as well as the smaller-scale vortex in ICE_{68}, can be expected to be more susceptible to tilting than their stronger, respectively broader-scale counterparts in RMN_{68} and $CBLAST_{68}$. In ICE_{68}, the susceptibility to tilting is potentially enhanced by the near-zero gradient of the skirt vorticity inside of 65 km. In Sec. 3.3 it will be shown that the tilt evolution is broadly consistent with these expectations. Furthermore, based on the results of Wong and Chan (2004), one can expect a more pronounced intensity decrease in ICE_{68} based on the radial scale of the vortex alone. The latter point needs to be borne in mind when attempting to attribute differences between ICE_{68} and RMN_{68} to their different representation of cloud microphysical processes.

3.2 Intensity evolution

An overview of the intensity evolution in our experiments is presented in Fig. 2. First, a brief account of the intensity evolution in a quiescent environment is given. The intensity evolution in RMN is described in some detail in RMN10. In CBLAST (Fig. 2(a)), the incipient TC slowly intensifies to 25 ms^{-1} in the first 20 h. A period of rapid intensification ensues during which the TC reaches an intensity of 53 ms^{-1} at 33 h. In the subsequent 20 h the TC consolidates and slightly intensifies

---

[8]Note that the temporal resolution of the data in Fig. 4 is 1 h. It is thus most likely that the vortex precession is undersampled.

to 56 ms^{-1}. Then, the TC continues to intensify at a moderate rate until it reaches a quasi-steady intensity of 80 ms^{-1} - 85 ms^{-1} at 80 h. In ICE (Fig. 2(b)), the TC intensifies to approx. 40 ms^{-1} at 30 h after a short gestation period. Very rapid intensification ensues and the intensity reaches

325   90 ms^{-1} at 50 h. The maximum, quasi-steady intensity of 95 ms^{-1} - 100 ms^{-1} is reached around 72 h.

In all experiments, intensity decreases after vertical wind shear is imposed. As in RMN10, all TCs are resilient to the detrimental impact of vertical wind shear. After a period of weakening the TCs re-intensify; particularly rapidly in RMN$_{54}$[9]. The re-intensification process in this experimental

330   configuration is discussed in some detail in RMN10 (their Sec. 6).

To facilitate the intercomparison of the intensity evolution in the various experiments, the intensity difference to the respective no-shear experiment is presented in Figs. 2(c) and 2(d). Time 0 h in these figures denotes the time when vertical wind shear is imposed in the respective experiment. In all warm-rain experiments (Fig. 2(c)), the characteristics of this *relative* weakening are similar in

335   the first 20 h. The only exception being that the weakening in CBLAST$_{54}$ is delayed by 4 h. This detail will be examined in section 3.6.2. After 20 h, the experiments with weaker TCs (RMN$_{54}$ and CBLAST$_{54}$) continue to weaken. In contrast, CBLAST$_{68}$ maintains its intensity difference for the next 20 h and RMN$_{68}$ re-intensifies. Based on these plots alone it might therefore be concluded that the weaker storms are more susceptible to shear. However, this is not necessarily the case here.

340   Note that 20 h after shear is imposed in RMN$_{54}$ and CBLAST$_{54}$ the respective reference TCs in quiescent environment are still rapidly intensifying. In contrast, the reference TCs in RMN$_{68}$ and CBLAST$_{68}$ intensify only slowly 20 h after vertical wind shear is imposed. Thus, the differences in the *relative* intensity evolution partly arise due to the differences in the contemporaneous evolution of the reference TC. This brief discussion illustrates one of the inevitable challenges to interpreting

345   different TC simulations in vertical wind shear.

The comparison of the RMN and ICE shear experiments is less complicated because the intensity evolution of the reference runs in quiescent environment is similar (Figs. 2(b) and 2(d)). A comparison of the intensity evolution in $_{10}$ICE$_{68}$ and ICE$_{68}$, respectively, clearly shows that the TCs in the ICE experiments are more susceptible to shear than their counterparts in the warm-rain experiments.

350   The differences between the relative weakening in $_{10}$ICE$_{68}$ and $_{10}$RMN$_{68}$, i.e. the experiments with imposed vertical shear of 10 ms^{-1}, is on average approx. 10 ms^{-1} before 16 h, and on average approx. 5ms^{-1} between 16 h and 36 h (Figs. 2(d)). After this time, it is no longer evident that the weakening in $_{10}$ICE$_{68}$ is more pronounced than in $_{10}$RMN$_{68}$.

For 15 ms^{-1} shear, the difference in the intensity evolution between the ice and warm-rain ex-

355   periments is striking. The maximum relative weakening in ICE$_{68}$ is -60 ms^{-1} (Figs. 2(d)). The TC reaches a minimum intensity of 35 ms^{-1} (Figs. 2(b)). For RMN$_{68}$, the respective values are -

---

[9]Because the focus of this study is on the structural changes of the TCs during the weakening phase, this experiment was discontinued at 84 h.

$25\ \mathrm{ms}^{-1}$ and $63\ \mathrm{ms}^{-1}$. Notwithstanding this distinct intensity evolution, it will be shown below that the structural changes in ICE_{68} and RMN_{68} are very similar. In particular, the pronounced weakening in ICE_{68} is associated with by far the most significant depression of inflow layer θ_e (sections 3.6 and 4.1). The evolution in ICE_{68} is thus consistent with the results of RMN10, i.e. the shear-induced frustration of inflow layer θ_e plays a crucial role in the intensity evolution in ICE_{68}. Furthermore, it will be argued in section 4.2 that this rapid weakening is consistent with the frictional spindown of an axisymmetric vortex due to a significant reduction of the inner-core convective mass flux.

3.3   Evolution of vortex tilt

Following RMN10, the tilt of the vortex is defined here as the vector difference between the vorticity centroids at 10 km and 1 km height. Details on the calculation of the vorticity centroids are given in RMN10.

A detailed examination of the tilt evolution in RMN_{68} was given in section 5.1 of RMN10. There, evidence was presented that the tilt evolution is governed to zero order by asymmetric-balance dynamics. The TC in RMN_{68} settles into a quasi-equilibrium tilt direction to the downshear-left (south) shortly after shear is imposed (approx. within 3 h). A quasi-equilibrium tilt direction may be achieved when the cyclonic precession of the tilted vortex cancels the differential advection by the vertical shear flow. This quasi-equilibrium vortex tilt can be described in a first approximation by the balanced dynamics of an initially barotropic, dry TC-like vortex (Jones, 1995; Reasor et al., 2004). In RMN_{68}, the tilt amplitude decreases while maintaining the quasi-equilibrium tilt direction. The TC virtually re-aligns within approx. 24 h, i.e. after this time the tilt amplitude is comparable to the tilt amplitude of the TC in the no-shear benchmark experiment (see Fig. 5 in RMN10). Once the tilt amplitude has decreased considerably, a high variability in the tilt direction ensues, indicative of a high-frequency precession of the vortex.

Figures 3 and 4 demonstrate that the general characteristics of the tilt evolution are similar in all of our experiments in the first 24 h - 30 h after vertical wind shear is imposed. All TCs are resilient during this time and the tilt direction is predominantly to the South ($180°$). In CBLAST_{68}, the maximum tilt magnitude, as well as the temporal tilt evolution, is very similar to that of RMN_{68}. The only exception being that the local maximum at 23 h is more pronounced and, thereafter, the tilt magnitude remains 3 km - 5 km larger. As can be expected from the discussion in Sec. 3.1, the weaker TCs in RMN_{54} and CBLAST_{54} clearly exhibit a larger tilt magnitude in the first 24 h than the more intense TCs in RMN_{68}, CBLAST_{68}, and ICE_{68}. Maximum tilt amplitudes reach 40 km in RMN_{54} and 30 km in CBLAST_{54}. Both TCs eventually re-align.

The most striking feature in the tilt evolution is the disruption of the TC vortex after 30 h in ICE_{68} (Fig. 3). Until this time the TC tends to re-align slowly: the local tilt maximum and minimum at 25 h and 30 h, respectively, are smaller than their respective predecessors at 9 h and 15 h. At 30 h, intensity has decreased by over $30\ \mathrm{ms}^{-1}$ as compared to the time when vertical wind shear is

imposed and has reached the smallest absolute value in all experiments (approx. 35 ms^{-1}, Fig. 2).
Based on the discussion in Sec. 3.1, it is plausible that the significantly weakened TC can no longer

395 withstand the differential advection associated with the vertical wind shear. Note that the distinct
weakening in the first 20 h precedes the disruption of the TC by more than 10 h. After 30 h, the
TC remains as a coherent entity with smaller vertical extent: the tilt as inferred from the vorticity
centroid at 9 km height instead of 10 km height does not exceed 35 km (not shown). Arguably, the
survival as a vertically less extensive system allows for the rapid re-intensification of the TC after

400 the inflow layer θ_e values have recovered (Sec. 4.1).

The tilt magnitude in $_{10}ICE_{68}$ remains below 10 km and quickly reduces to values smaller than
6 km after 12 h. Despite this small tilt magnitude a southerly tilt direction is preferred until late in
the experiment. Although the evolution of the tilt magnitude is similar in $_{10}RMN_{68}$, the tilt direction
in $_{10}RMN_{68}$ exhibits more variability after 30 h when the tilt magnitude is small (not shown).

405 **3.4 SBC formation and downward flux of low-θ_e air into the inflow layer**

A metric for the downward flux of low-θ_e air into the inflow layer (DFX) has been defined in RMN10
(their Sec. 4.2.1) as

$$DFX \equiv w_- \theta'_e, \tag{4}$$

where w_- denotes downward vertical motion and θ'_e the perturbation from the azimuthal mean of

410 θ_e. DFX is evaluated at 1.5 km, the approximate top of the axisymmetric inflow layer.

The time-averaged structure of the SBC, represented by low-level upward motion, and the dis-
tribution of DFX shortly after the time when vertical wind shear is imposed is depicted in Fig. 5.
In this early stage of the evolution, the general structure of the SBC and the distribution of DFX is
consistent in all experiments. The SBC forms in the downshear-right quadrant extending radially

415 outwards to 150 km - 200 km. Small to moderate DFX values occur over a broad, banded region
downwind of the SBC, from the downshear quadrant through downshear-left, and into the upshear
quadrant. In all experiments, azimuthal vertical cross-sections (as Fig. 18 in RMN, not shown here)
indicate that the associated downdrafts form underneath the helical updrafts of the SBC.

It is of interest to note that the SBCs in RMN_{54}, ICE_{68}, and $_{10}ICE_{68}$, respectively, extend further

420 into the upshear quadrant than their counterparts in RMN_{68}, $CBLAST_{68}$, and $CBLAST_{54}$. In the
former experiments, the tilt direction at early times exhibits a greater downshear (westerly) com-
ponent than in the latter experiments (Fig. 4). The low-level vorticity anomaly associated with the
tilted vortex can thus be expected to extend into the upshear quadrant. RMN10 have shown evidence
that frictional convergence due to the low-level vorticity anomaly associated with the tilted vortex

425 contributes to the forcing of the SBC. The correlation of the SBC formation location and the tilt
direction in our experiments presented here provides further support for RMN10's interpretation.

A distinct maximum of DFX is found in the upshear quadrant close to the eyewall. This maximum
is most pronounced in the ICE experiments (Fig. 5(e) and 5(f)). In RMN10, this DFX maximum

13

was not given special attention. A pronounced maximum in the upshear quadrant occured in the 20mps case of RMN10 (their Fig. 10(d)). RMN10 further noted a localized region of downdrafts in the upshear region close to the eyewall after the TCs in the 10mps and 15mps cases have re-aligned (their Fig. 11(a) and associated discussion).

The DFX maximum is located at the downwind end of the banded region of positive DFX values. A pronounced θ_e depression is found at the top of the inflow layer in this region (not shown). Large, negative values of θ_e' therefore contribute to high values of DFX (Eq. 4). Downward motion into the inflow layer, however, is particularly strong in this region also (not shown). A preliminary examination of the distributions of vertical motion, hydrometeors, and θ_e suggests that the downdrafts close to the eyewall may form by evaporation of precipitation falling out of the tilted eyewall. To us, however, it is not clear whether the more pronounced localized maximum in the ICE experiments is solely due to the inclusion of ice microphysics or to what extent the differences in the radial structure of the TC vortex contribute. Clearly, more research is needed to clarify the formation mechanism of these downdrafts and the relative importance of the confined DFX maximum and the broad region of moderate DFX for TC intensity evolution.

3.5   Vortex-tilt induced dynamic instability?

A non-linear, Kelvin-Helmholtz type instability in the inner core of a tilted, dry TC-like vortex has been found in a numerical experiment by Reasor et al. (2004, their Sec. 5a). In their experiment, this instability contributed to enhanced localized, three-dimensional mixing. Such mixing is one pathway to dissipate kinetic energy in the TC's inner core. The role of this mixing for the intensity evolution of TCs in vertical wind shear is hitherto unexplored.

The necessary condition for such an instability is that the gradient Richardson number, $\mathcal{R}$, drops below unity (Abarbanel et al., 1986). Here, $\mathcal{R}$ is calculated as

$$\mathcal{R} = N^2/((du/dz)^2 + (dv/dz)^2), \tag{5}$$

where N is the (dry) vertical static stability, and u and v are the radial and tangential wind components[10], respectively. The tilt of the vortex may lead to a high *local* vertical shear of the swirling winds in the inner core. Thus, in such regions, the gradient Richardson number may reach small values.

In all of our (moist) TC experiments, the potential for a Kelvin-Helmholtz type instability and the associated three-dimensional, turbulent mixing in the inner core is an element of vertical-shear interaction. Underneath the eyewall and the SBC, $\mathcal{R} < 1$ is an ubiquitous feature within the layer of strong, frictionally-driven inflow (not shown). Above this inflow layer, localized regions of $\mathcal{R} < 1$ occur, at least temporarily, in all experiments presented in this study within the first 6 h after shear

---

[10]Normally, the definition of $\mathcal{R}$ involves the zonal and meridional wind components. Our calculation of $\mathcal{R}$ is equivalent to this definition.

is imposed. These regions are located within the eyewall in the downshear-left to upshear quadrant (exemplified in Fig. 6 for RMN_{68} and ICE_{68}). This feature is most pronounced in RMN_{68} and least pronounced in RMN_{54}, as might be expected for the weaker vortex in RMN_{54}. The regions of $\mathcal{R} < 1$ are frequently located radially inwards (within 20 km - 30 km) of regions of high DFX (exemplified in Fig. 6). Due to this proximity, it seems justified to hypothesize that enhanced mixing associated with the tilt-induced instability locally modifies the downward flux of low-θ_e air into the inflow layer. A quantitative diagnostic of this mixing process is deferred to future work.

3.6   Inflow layer θ_e depression

3.6.1 θ_e depression outside of the eyewall

A snapshot of the height-averaged inflow layer θ_e distribution after 5 h into the shear experiments is presented in Fig. 7. As can be expected from the DFX patterns discussed above, the inflow layer θ_e distribution is similar in all experiments at this time: Low-θ_e air wraps cyclonically from the downshear quadrant into the upshear quadrant. Also evident in all cases is the pronounced wavenumber 1 signature of the SBC in the vertical motion field at low levels above the inflow layer.

To facilitate the intercomparison of the experiments we consider now the deviation from the axisymmetric mean θ_e distribution at the time when shear is imposed in the respective experiment (Fig. 8). This figure depicts time-averaged values from 4 h - 9 h after shear is imposed. In all cases the inflow layer θ_e values outside of the inner-core updrafts are significantly depressed. A depression of up to 15 K can be found in RMN_{68}, RMN_{54}, and ICE_{68}. Minimum θ_e values are generally found to the southeast of the centre (upshear to downshear-left). This location is consistent with the DFX maximum in this region and the continuous depression of θ_e values along the spiralling inflow leg, as hypothesised by RMN10 (their Fig. 11a). The inflow layer θ_e depression extends into the downshear-right quadrant also, outwards to a radius of 100 km - 150 km. In the absence of downward flux of low θ_e in this region (cf. Fig. 5) the inflow layer θ_e values gradually recover while air parcels circle from the upshear quadrant to the upshear-right quadrant.

The inflow layer θ_e depression outside of the eyewall in the CBLAST experiments is less pronounced than in the comparable RMN experiments. While the minima in RMN exceed -13 K, the minima in CBLAST have values of approx. -10 K. This less pronounced θ_e depression is consistent with smaller average DFX in $CBLAST_{68}$ and $CBLAST_{54}$ as compared to RMN_{68} and RMN_{54}, respectively (Fig. 5). The smaller DFX values in CBLAST are associated with a weaker general downdraft activity (see section 3.7 and Fig. 10 for supporting evidence).

In the ICE experiments, the spatial pattern of the θ_e depression is radially more confined than in the warm-rain experiments. This is consistent with the DFX pattern. As discussed at the end of Sec. 3.4, it is not evident to us to what extent this greater radial confinement can be attributed to differences in the cloud microphysics or to differences in the radial structure of the TC vortices.

15

3.6.2 θ_e depression underneath the inner-core updrafts

An axisymmetric view of the inflow layer and eyewall θ_e distribution is presented in RMN10. In this axisymmetric view a tongue of low-θ_e air effectively intrudes into the inflow layer from above and radially inwards towards the eyewall. The θ_e values of air rising in the eyewall of the sheared TCs are several degrees smaller than in the experiment without vertical shear (Fig. 9 in RMN10). The same general characteristics of the axisymmetric inflow layer and adjacent eyewall structure are found in the additional experiments considered in this study (not shown). When viewed from the simplified perspective of an idealised Carnot-cycle a weakening of the sheared TCs can thus be expected. As noted in RMN10, however, it is an open question whether an axisymmetric viewpoint is sufficient in the presence of pronounced wave-number 1 asymmetries in the inflow layer θ_e distribution and the eyewall updrafts of a TC in vertical wind shear.

In the present study we complement the axisymmetric view by the examination of the horizontal distribution of inflow layer θ_e and low-level eyewall updrafts. For the following discussion the eyewall updrafts are defined as the contiguous region within the 1 ms^{-1} vertical velocity isotach near the centre in Fig. 8. We consider the θ_e values within this region to be a good approximation for the θ_e values of air rising out of the boundary/ sub-cloud layer in the eyewall updrafts. Upon examining the results, it is obvious that in all cases the inner-core updrafts exhibit a pronounced wave-number 1 asymmetry and that the eyewall is not closed.

By visual inspection we estimate the average θ_e depression underneath the eyewall (averaged from 4 h - 9 h) to be 0 K for CBLAST$_{54}$, 2 K - 3 K for RMN$_{68}$ and CBLAST$_{68}$, 3 K - 5 K for RMN$_{54}$ and $_{10}$ICE$_{68}$, and 6 K- 7 K for ICE$_{68}$. These values correlate well with the intensity evolution of the respective TCs. The TC in CBLAST$_{54}$ does not weaken until 7 h after shear is imposed (Fig. 2(c)). The TCs in RMN$_{68}$ and CBLAST$_{68}$ show a very similar weakening in the first 12 h while RMN$_{54}$ and $_{10}$ICE$_{68}$ exhibit slightly faster weakening rates. The pronounced and rapid weakening of the TC in ICE$_{68}$ is associated with the most pronounced depression of θ_e underneath the eyewall. This correlation supports RMN10's result that the intensity evolution of resilient TCs in vertical shear is governed to first order by the systematic depression of θ_e in the inflow layer.

The inflow layer θ_e depression *outside* of the eyewall in CBLAST$_{68}$ is less pronounced than in RMN$_{68}$. The θ_e depression underneath the eyewall, however, is very similar in both experiments. Consistently, the intensity decrease is very similar in CBLAST$_{68}$ and RMN$_{68}$ in the first 12 h. It can therefore be inferred that the replenishment of inflow air spiralling towards the eyewall is more complete in RMN than in CBLAST. As discussed in the Introduction, the smaller value of C_D in CBLAST may lead to weaker frictional inflow as compared to RMN and thus to a longer replenishment time. Here, this effect of a smaller C_D value is apparently overruled by the reduced extraction of heat from the ocean surface due to a smaller value of C_K. It is difficult to examine this aspect in RMN$_{54}$ and CBLAST$_{54}$ because the θ_e depression underneath the eyewall is different at this early time in the experiment.

16

The replenishment time of air with depressed θ_e values may depend considerably on the *azimuthal*
location. The radial velocity averaged over the lowest 1 km exhibits a pronounced wave-number 1
asymmetry in all experiments (Fig. 8). In the downshear semicircle the maximum height-averaged
radial inflow is approx. 20 ms^{-1} while in the upshear semicircle the height-averaged radial velocity
is very small or is even directed *outwards* (e.g. in RMN54 (Fig. 8(c))). Figure 8 indicates that
the bulk of the depressed inflow layer θ_e spirals around the centre before entering the inner core
updrafts in the downshear-right quadrant (e.g. Figs. 8(a) and 8(f)). In RMN$_{54}$ and ICE$_{68}$, in contrast,
it is indicated that low-θ_e air from the downshear quadrant enters the eyewall updrafts on a much
more direct pathway in the downshear to downshear-left quadrant also (Figs. 8(c) and 8(e)). The
replenishment of inflow layer θ_e along this more direct pathway can be expected to be less complete
than along the longer inflow spiral. In the presence of a pronounced wave-number 1 asymmetry of
the inflow, it stands to reason that the (azimuthal) *location* of the flushing of the inflow layer with
low-θ_e air may be of importance for the intensity evolution also, and not only the magnitude of the
θ_e depression in the azimuthal mean.

3.7 Vertical motion characteristics

The formation of the SBC and the associated downdrafts that flush low-θ air into the inflow layer
are two central aspects of RMN10's framework. We here examine the general characteristics of
vertical motion in our suite of experiments using so-called contoured frequency by altitude diagrams
(CFADs Yuter and Houze, 1995). These diagrams depict the frequency of the occurrence of vertical
motion of a given magnitude, here binned in 0.5 ms^{-1} intervals, within a given region and at a given
altitude. It is very difficult to focus specifically on the SBC and on regions where shear-induced
downdrafts form. We therefore consider all vertical motion within a radius of 160 km.

A comparison of the RMN and ICE experiments is presented in Fig. 9. Without vertical wind shear
(Figs. 9(a) and 9(b)) strong up- and downdrafts occur more frequently in the ICE experiment. Under
the influence of vertical shear (Figs. 9(c) and 9(d)), the frequency distribution broadens considerably
below 5 km - 6 km as compared to the respective no-shear experiment. For both, the warm rain
and ice microphysics configurations, vertical wind shear increases the frequency of the strongest up-
and downdrafts at midlevels and below. At upper levels the increase of downdraft frequency is less
pronounced and the frequency of strong updrafts tends to decrease, except for the strongest updrafts
in ICE$_{68}$. It is evident also that strong downdrafts below 5 km occur considerably more frequently in
ICE$_{68}$ than in RMN$_{68}$ (cf. Figs. 9(c) and 9(d)). The more pronounced downdraft activity in the ICE
experiments is consistent with the tenet that the cooling associated with the melting of ice particles
may initiate or strengthen existing downdrafts (Srivastava, 1987).

In CBLAST, the imposed vertical wind shear leads to a broadening of the frequency distribution
also (not shown). The differences between CBLAST and RMN experiments are less pronounced
than between ICE and RMN. The differences are depicted in Fig. 10 as the ratio of the frequen-

17

570　cies in RMN$_{68}$ and CBLAST$_{68}$ (Fig. 10(a)) and RMN$_{54}$ and CBLAST$_{54}$ (Fig. 10(b)). The results are very similar for RMN and CBLAST without imposed vertical shear (not shown). Apparently, the frequency of the strongest downdrafts is more than 275 % greater in RMN than in CBLAST. Strong updrafts tend to be more frequent in RMN also, in particular so in RMN$_{54}$ as compared to CBLAST$_{54}$.

575　　Differences in the thermodynamic properties of the ambient air in which downdrafts occur may contribute to the observed differences in downdraft activity. The strength of a downdraft depends, inter alia, on the buoyancy difference between the descending air parcel and the ambient air along the parcel's downward path. A vertically integrated measure of this buoyancy difference is the downdraft convective available potential energy (DCAPE, Emanuel, 1994, his Sec. 6.3). The derivation of

580　DCAPE assumes the following two-stage process. First, evaporation of precipitation cools an air parcel isobarically through a wet-bulb process, i.e. until saturation is reached. Then, the parcel descends pseudo-adiabatically with just enough evaporation to keep the parcel saturated.

　　We have calculated DCAPE using the azimuthal mean soundings at the time when shear is imposed. Because it is not entirely clear which radius is most appropriate to examine the downdrafts

585　underneath the SBC we considered a number of different radii and radial averages between 60 km and 150 km (not shown). For all of these regions, a clear relationship between the DCAPE values and the downdraft activity, respectively the downward flux of low-θ_e air into the inflow layer, is not found. In particular, DCAPE values below 500 hPa in CBLAST$_{54}$ are higher than in RMN$_{54}$, *in contrast* to the more pronounced downdraft activity in RMN$_{54}$.

590　　Apparently, consideration of solely thermodynamic properties of the air in which the downdrafts occur is insufficient to explain the observed differences in downdraft activity. We propose the following alternative explanation that focuses on the dynamic coupling of the convection with the frictional boundary layer. First, we note that the weaker downdrafts in CBLAST$_{68}$ and CBLAST$_{54}$ are associated with weaker updraft activity. This may be expected because a prominent downdraft formation

595　mechanism is the evaporation of precipitation that is formed in the updrafts and falls into unsaturated air. Both the smaller value of C_D and C_K in CBLAST may contribute to weaker updrafts. Ascent out of the boundary layer forced by frictional convergence, either underneath the eyewall or underneath the vorticity anomaly associated with the tilt of the outer vortex (RMN10, their Fig. 17), can be expected to decrease for decreasing C_D. For example, in simple Ekman pumping theory the vertical

600　motion at the top of the boundary layer is proportional to $\sqrt{C_D}$ (e.g. Holton, 2004, his Eq. 5.38). The smaller value of C_K in CBLAST decreases the rate by which heat is extracted from the ocean surface. These reduced surface fluxes destabilise the boundary layer in CBLAST to a lesser extent than in RMN. Less vigorous updrafts can be expected to occur in such a more stable stratification. Our foregoing argument is supported by the results of the CBLAST and RMN no-shear experiments

605　(not shown). Without vertical shear, the activity of *transient* rain bands and the associated localized downward flux of low θ_e into the inflow layer in CBLAST are also less pronounced than in the

18

no-shear RMN experiment.

In all experiments, vertical wind shear increases the frequency of moderate to strong downdrafts. It is clear that CBLAST has the lowest frequency of strong downdrafts and that ICE has the highest frequency. The downdraft activity as seen in the CFADs is consistent with the magnitude of the inflow layer θ_e depression outside of the eyewall (cf. Fig.8). Therefore, the examination of the CFADs provides additional support for the hypothesis that the distinct depression of the inflow layer θ_e values are caused by downdrafts induced by the imposed vertical wind shear.

4 A closer look at the ICE$_{68}$ experiment

The weakening of the TC in ICE$_{68}$ is much more pronounced than in the comparable warm-rain experiments RMN$_{68}$ and CBLAST$_{68}$. In the previous sections it has been shown that the general structural changes in the first 20 h are nevertheless very similar in all experiments. We now take a closer look at ICE$_{68}$ to further confirm that the intensity evolution in this case is consistent with the shear-induced thermodynamic modification of the inflow layer. First, the inflow layer θ_e distribution is examined during periods of distinct intensity changes. Then, we will provide evidence based on axisymmetric spindown theory that the rapid weakening in the first 20 h is consistent with the spindown of the TC vortex due to a significant decrease of the inner core convective mass flux.

4.1 Intensity evolution and inflow layer θ_e

It has been shown in section 3.6 (Fig. 7(e)) that the rapid weakening is associated with a significant depression of inflow layer θ_e soon after shear is imposed. Here we emphasize that a significant part of the depressed θ_e-air apparently intrudes from the downshear quadrant into the inner-core updrafts on a direct pathway (Fig. 11(a), at 7 h). Over half of the area underneath the inner-core updrafts at this time has θ_e values lower than 355 K, as compared to approx. 363 K before shear is imposed (not shown). Along with this significant frustration of the θ_e values in the inner-core region the vertical mass flux at midlevels (5 km) decreases in the first 10 h by 60 % from 50×10^6kg s^{-1} to approx. 20×10^6kg s^{-1} (not shown).

We now consider the two distinct, short-lived local intensity maxima at 22 h and 44 h, prominent features of the intensity evolution in ICE$_{68}$ (Fig. 2(b), the maxima are found at 64 h and 86 h because this figure includes the 42 h spinup period). Both periods of temporary re-intensification are preceded by relatively high inflow layer θ_e values in the downshear to downshear-right quadrants while the very pronounced θ_e depression at these times is mostly confined to the upshear semicircle (at 20 h (Fig. 11(b)) and at 40 h (Fig. 11(d))). Due to the distinct wave-number 1 inflow asymmetry discussed previously (Fig. 8), it can be expected that, at these times, the eyewall updrafts are fed to a large extent by the relatively high-θ_e air in the downshear semicircle. Eyewall θ_e values may then temporarily increase and the TC may intensify. The temporary intensification ensues until the very

low θ_e air from the upshear semicircle wraps around the centre and limits considerably the supply of relatively high θ_e (exemplified at 23 h (Fig. 11(c)) and at 45 h (Fig. 11(e))).

At the end of our experiment a robust re-intensification is indicated in the intensity time series (Fig. 2(b)). As in the experiments examined in RMN10, this final re-intensification is associated with an almost complete recovery of the inflow layer θ_e (Fig. 11(f)).

As indicated in Figs. 11(b) - 11(e), low-θ_e air in the inflow layer may wrap around the centre into the downshear-right quadrant. This low-θ_e air tends to suppress the convection of the SBC. Furthermore, after 20 h in ICE_{68} the vortex tilt is no longer in the approximate left-of-shear equilibrium direction but starts to precess. In accordance with this precession, the vorticity anomaly associated with the tilt of the outer vortex then starts to move also and thus no longer provides persistent forcing for the SBC in the downshear-right quadrant. It is interesting to note that a narrow band of convection preferably occurs in the downshear quadrant at these later times (Figs. 11(b) - 11(e)). Frequently, one observes significant downward flux of low θ_e associated with this remnant SBC (not shown).

4.2 A timescale for vortex spindown

Within the simplified framework of an idealised Carnot cycle, and based on the idea that environmental vertical wind shear leads to the frustration of such a thermodynamic cycle, Tang and Emanuel (2010) have derived a theory for the storm's reduced *steady-state* intensity. Such a theory, however, does not provide information about the *temporal evolution* of storm intensity, i.e. how rapidly a TC weakens. A well-known concept for the weakening of a TC is the axisymmetric, frictionally-induced spindown of the TC vortex. Frictional convergence forces ascent out of the inflow layer. When the vertical convective mass flux is smaller than the frictionally forced vertical mass flux, some of the air has to diverge above the inflow layer due to mass continuity (Willoughby, 1979). Under the assumption that air parcels approximately conserve their angular momentum above the frictional inflow layer, this divergence implies a decay of the tangential winds, i.e. the TC weakens.

A timescale for the frictional spindown of an *axisymmetric* vortex *without* convective mass flux has been derived by Elliassen and Lystad (1977). Their model assumes a neutral stratification above the layer of strong frictional inflow which is a reasonable assumption in the inner core of a TC because isosurfaces of θ_e and angular momentum are approximately congruent in this region. Montgomery et al. (2001) have verified by numerical experiments that the theory gives reasonable results for the spindown of TC-like vortices, even beyond the formal validity of the theory. The half-time t_{half}, i.e. the time that is required to reduce the initial tangential velocity v by a factor of 2, is given by Elliassen and Lystad's theory as

$$t_{half} = \frac{H-h}{\chi^2 C_D v}. \tag{6}$$

Here, H is the fluid depth, h the height of the boundary layer, and χ a reduction factor defined by Elliassen and Lystad as the ratio of the tangential winds at the top of the surface layer to the tangential

winds at the top of the Ekman layer. Estimating $H - h = 10^4$ m, $\chi = 0.8$, and using $C_D = 3.8 \times 10^{-3}$ from Deacon's formula with $v = 68$ ms^{-1} yields a half-time $t_{half} = 16.8$ h.

The weakening of the TC in ICE$_{68}$ is remarkable: intensity decreases from 68 ms^{-1} at 42 h to

680   33 ms^{-1} at 68 h (Fig. 2(b)), corresponding to a weakening rate of 35 ms^{-1} in 26 h; or a half-time of approx. 25 h. This value is consistent with a *partial* shutdown of the convective mass flux. As noted above, concurrently with the frustration of the inflow layer θ_e and the rapid weakening, the vertical mass flux at 5 km height decreases by approx. 60%. Consequently, it can be argued that the significant reduction of the convective vertical mass flux by the severe depression of the inflow layer

685   θ_e values broadly governs the rapid weakening in ICE$_{68}$.

5   Conclusions

In the light of a new framework developed in a recent study (RMN10), the current study further examines the evolution of TCs exposed to environmental vertical wind shear. The new framework has been developed based on idealized numerical experiments for which we have deliberately chosen

690   a simple set of physical parameterisations to minimize the complexity of the problem. In the current study, we survey and diagnose five additional numerical experiments with some modifications of the experimental setup to assess the robustness of our previous results.

The modifications of the experimental setup focus on parameters that are important for structure change and intensity evolution of numerically simulated TCs and the storms' evolution in vertical

695   wind shear, discussed in some detail in the Introduction in Sec. 1.2. Specifically, in comparison to RMN10, we here consider weaker, but still mature TCs; employ values for the exchange coefficients of surface heat and momentum fluxes that are in better agreement with recent observational results; and complement our previous warm-rain experiments with experiments that employ an ice microphysics scheme.

700   The ability of TC-like vortices to withstand the differential advection by vertical wind shear and to eventually re-align depends on the radial profile of the swirling winds (discussed in detail in Sec.3.1). Some differences in this radial structure arise in the individual experiments *before* interacting with the imposed vertical wind shear. The most notable differences are found in the experiment with ice microphysics in which the TC, inter alia, features a radius of maximum winds that is approx. 25 %

705   smaller than in the warm-rain experiments. Differences in the radial vortex structure complicate the attribution of differences in the TC evolution to, e.g., the inclusion of ice microphysics alone.

The differences in the vortex structure notwithstanding, in all experiments the TCs exhibit the same general structural changes when exposed to vertical wind shear. The structural changes are consistent with RMN10's new framework and comprise a vortex tilt predominantly to the downshear-

710   left for 20 h - 24 h, the formation of a pronounced wave-number 1 convective asymmetry *outside* of the eyewall (reminiscent of a stationary band complex), and downward flux of low-θ_e air into the

21

inflow layer in the downshear-left semicircle. A significant depression of the inflow layer θ_e values ($\mathcal{O}(10\ K)$) occurs in all experiments.

Furthermore, for all experiments the potential for a non-linear, Kelvin-Helmholtz type instability in the inner core of the tilted TC-vortex is diagnosed. Such an instability would contribute to enhanced dissipation of kinetic energy and may modify the flux of low-θ_e air into the inflow layer. A quantitative analysis of the mixing process associated with the potential instability, however, is deferred to future work.

Two additional diagnostics are considered in the current study that have not been considered in RMN10, namely the θ_e values underneath the *asymmetric* inner-core updrafts, and so-called contoured frequency by altitude diagrams to examine the general characteristics of vertical motion. The magnitude of the θ_e depression underneath the *asymmetric* inner-core updrafts early in the respective shear experiment correlates well with the ensuing weakening of the TC, supporting the idea that it is the depression of the inflow layer θ_e that governs the intensity evolution to first order. For all experiments, vertical wind shear increases the frequency of strong downdrafts as compared to the no-shear experiments. The magnitude of the θ_e depression *outside* of the eyewall is consistent with the frequency of strong downdrafts, supporting the idea that it is the shear-induced downdrafts that flush low-θ_e air into the inflow layer. Consequently, both additional diagnostics corroborate RMN10's framework.

In one of our experiments employing ice microphysics, a very rapid weakening of the TC occurs. This intensity evolution is distinct from the intensity evolution in our warm-rain experiments. Therefore, a question may naturally arise whether ice microphysics, as represented in the RAMS model, introduces an important mechanism for intensity change that is not considered in RMN10's framework. As noted above, the structural changes caused by the vertical wind shear in the experiment with ice microphysics are very similar as in the warm-rain experiments. In the ice experiment, the general downdraft activity, the flux of low-θ_e air into the inflow layer, and the θ_e depression underneath the inner-core updrafts are all the most pronounced in our suite of experiments. The inner-core θ_e depression that accompanies the initial rapid weakening is more than twice as high than in the comparable experiments employing warm-rain microphysics (6 K - 7 K as compared to 2 K - 3 K). Axisymmetric spindown theory (Elliassen and Lystad, 1977; Montgomery et al., 2001) further supports the hypothesis that the rapid initial weakening is due to a substantial decrease of the convective mass flux associated with the significant depression of the inflow layer θ_e by shear-induced downdrafts. In addition, we have documented a close relationship between the evolution of the inflow layer θ_e values and two transient intensity maxima that occur at 22 h and 44 h after vertical wind shear is imposed. The final re-intensification of the TC in this experiment, as in RMN10, is associated with a near-complete replenishment of the inflow layer θ_e values also.

Based on the evidence presented here, we conclude that RMN10's framework for the intensity modification of TCs in vertical wind shear is robust to the presented changes in the setup of the

22

numerical experiment. We advocate further study and tests of this framework with case studies and
real atmospheric data.

References

Abarbanel, H. D. I., Holm, D. D., Marsden, J. E., and Ratiu, T.: Nonlinear stability of incompressible stratified flow, Phil. Trans. Roy. Soc., A318, 349–409, 1986.

Bell, M. M.: Air – sea enthalpy and momentum exchange at major hurricane wind speeds, Ph.D. thesis, Naval Postgraduate School, Monterey, California, USA, 2010.

Bender, M. A.: The effect of relative flow on the asymmetric structure in the interior of hurricanes, J. Atmos. Sci., 54, 703–724, 1997.

Black, P. G., D'Asaro, E. A., Drennan, W. M., French, J. R., Niiler, P. P., Sanford, T. B., Terrill, E. J., Walsh, E. J., and Zhang, J. A.: Air-sea exchange in hurricanes: Synthesis of observations from the Coupled Boundary Layer Air-Sea Transfer experiment, Bull. Am. Meteorol. Soc., 88, 357–374, 2007.

Braun, S. A. and Tao, W. K.: Sensitivity of high-resolution simulations of Hurricane Bob (1991) to planetary boundary layer parameterizations, Mon. Wea. Rev., 128, 3941–3961, 2000.

Bui, H. H., Smith, R. K., Montgomery, M. T., and Peng, J.: Balanced and unbalanced aspects of tropical-cyclone intensification, Q. J. R. Meteorol. Soc., 135, 715–1731, 2009.

Cotton, W. R. and Coauthors: RAMS 2001: Current status and future directions, Meteor. Atmos. Phys., 82, 5–29, 2003.

DeMaria, M.: The effect of vertical shear on tropical cyclone intensity change, J. Atmos. Sci., 53, 2076–2088, 1996.

Elliassen, A. and Lystad, M.: On the Ekman layer in a circular vortex: A numerical and theoretical study., Geophys. Norv., 31, 1977.

Emanuel, K. A.: Atmospheric convection, pg. 172, Oxford University Press, New York, 1994.

Fovell, R. G., Corbosiero, K. L., and Kuo, H.-C.: Cloud Microphysics Impact on Hurricane Track as Revealed in Idealized Experiments, J. Atmos. Sci., 66, 1764–1778, 2009.

Frank, W. M. and Ritchie, E. A.: Effects of vertical wind shear on the intensity and structure of numerically simulated hurricanes, Mon. Wea. Rev., 129, 2249–2269, 2001.

Hill, G. E.: Factors controlling the size and spacing of cumulus clouds as revealed by numerical experiments, J. Atmos. Sci., 31, 646–673, 1974.

Holton, J.: An introduction to dynamic meteorology, pg 132, AcademicPress, London, 2004.

Jones, S. C.: The evolution of vortices in vertical shear. I: Initially barotropic vortices, Q. J. R. Meteorol. Soc., 121, 821–851, 1995.

Kessler, E.: On the distribution and continuity of water substance in atmospheric circulations, Meteor. Monogr. 32, Amer. Meteor. Soc., 1969.

Lilly, D. K.: On the numerical simulation of buoyant convection, Tellus, 14, 148–172, 1962.

Meyers, M., Walko, R., Harrington, J., and Cotton, W.: New RAMS cloud microphysics prameterization. Part II: The two-moment scheme., Atmos. Res., 45, 3–39, 1997.

Montgomery, M. T., Snell, H. D., and Yang, Z.: Axisymmetric Spindown Dynamics of Hurricane-like Vortices, J. Atmos. Sci., 58, 421–435, 2001.

Montgomery, M. T., Smith, R. K., and Nguyen, S. V.: Sensitivity of tropical cyclone models to the surface drag coefficient, Q. J. R. Meteorol. Soc., 136, 1945–1953, 2010.

Pielke, R. A. and Coauthors: A comprehensive meteorological modeling system – RAMS, Meteor. Atmos.

Phys., 49, 69–91, 1992.

Reasor, P. D., Montgomery, M. T., and Grasso, L. D.: A new look at the problem of tropical cyclones in vertical shear flow: Vortex resiliency, J. Atmos. Sci., 61, 3–22, 2004.

800   Riemer, M. and Montgomery, M. T.: Simple kinematic models for the environmental interaction of tropical cyclones in vertical wind shear, Atmos. Chem. Phys., 11, 9395–9414, http://www.atmos-chem-phys.net/11/9395/2011/, 2011.

Riemer, M., Montgomery, M. T., and Nicholls, M. E.: A new paradigm for intensity modification of tropical cyclones: thermodynamic impact of vertical wind shear on the inflow layer, Atmos. Chem. Phys., 10, 3163–
805   3188, http://www.atmos-chem-phys.net/10/3163/2010/, 2010.

Schecter, D. A. and Montgomery, M. T.: On the symmetrization rate of an intense geophysical vortex, Dyn. Atmos. Oceans, 37, 55–88, 2003.

Smagorinsky, J.: General circulation experiments with the primitive equations, Mon. Wea. Rev., 91, 99–164, 1963.

810   Smith, R. K. and Thomsen, G. L.: Dependence of tropical-cyclone intensification on the boundary-layer representation in a numerical model, Q.J.R. Meteorol. Soc., 136, 1671–1685, 2010.

Smith, R. K., Montgomery, M. T., and Thomsen, G.: Sensitivity of tropical cyclone models to the surface drag coefficient in different boundary-layer schemes, Q.J.R. Meteorol. Soc., p. in review, 2011.

Srivastava, R. C.: A Model of Intense Downdrafts Driven by the Melting and Evaporation of Precipitation, J.
815   Atmos. Sci., 44, 1752–1774, 1987.

Tang, B. and Emanuel, K. A.: Midlevel ventilation's constraint on tropical cyclone intensity, J. Atmos. Sci., 67, 1817–1830, 2010.

Tripoli, G. J. and Cotton, W. R.: The use of ice-liquid water potential temperature as a thermodynamic variable in deep atmospheric models, Mon. Wea. Rev., 109, 1094–1102, 1981.

820   Verlinde, J., Flatau, P., and Cotton, W.: Analytical solutions to the collection growth equation: Comparison with approximate methods and application to cloud microphysics parameterization schemes, J. Atmos. Sci., 47, 2871–2880, 1990.

Walko, R., Cotton, W., Harrington, J., and Meyers, M.: New RAMS cloud microphysics parameterization. Part I: The single-moment scheme, Atmos. Res., 38, 29–62, 1995.

825   Willoughby, H. E.: Forced secondary circulations in hurricanes, J. Geophys. Res., 84, 3173–3183, 1979.

Willoughby, H. E., Marks, F. D., and Feinberg, R. J.: Stationary and moving convective bands in hurricanes, J. Atmos. Sci., 41, 3189–3211, 1984.

Wong, M. L. M. and Chan, J. C. L.: Tropical cyclone intensity in vertical wind shear, J. Atmos. Sci., 61, 1859–1876, 2004.

830   Yuter, S. E. and Houze, R. A.: Three-Dimensional Kinematic and Microphysical Evolution of Florida Cumulonimbus. Part II: Frequency Distributions of Vertical Velocity, Reflectivity, and Differential Reflectivity, Mon. Wea. Rev., 123, 1941–1963, 1995.

Zhang, J. A., Black, P. G., French, J. R., and Drennan, W. M.: First direct measurements of enthalpy flux in the hurricane boundary layer: The CBLAST results, Geophys. Res. Lett., 35, 2008.

Table 1. Overview of the experiments that are considered in this study. The experiments RMN$_{68}$ and $_{10}$RMN$_{68}$ are described in detail in RMN10. In column C_K, 'Deacon' denotes that Deacon's formula (see section 2.3) is used to determine the exchange coefficients. The last column gives the TC's intensification rate just before vertical shear is imposed.

Experiment	'initial' intensity [ms^{-1}]	C_K	C_K/C_D	microphysics	shear [ms^{-1}/12 km]	preceding int. rate [ms^{-1}/h]
RMN$_{68}$	68	Deacon	1	warm	15	1.8
$_{10}$RMN$_{68}$	68	Deacon	1	warm	10	1.8
RMN$_{54}$	54	Deacon	1	warm	15	0.0
CBLAST$_{68}$	68	1.16×10^{-3}	0.65	warm	15	1.1
CBLAST$_{54}$	54	1.16×10^{-3}	0.65	warm	15	0.0
ICE$_{68}$	68	Deacon	1	ice	15	2.5
$_{10}$ICE$_{68}$	68	Deacon	1	ice	10	2.5
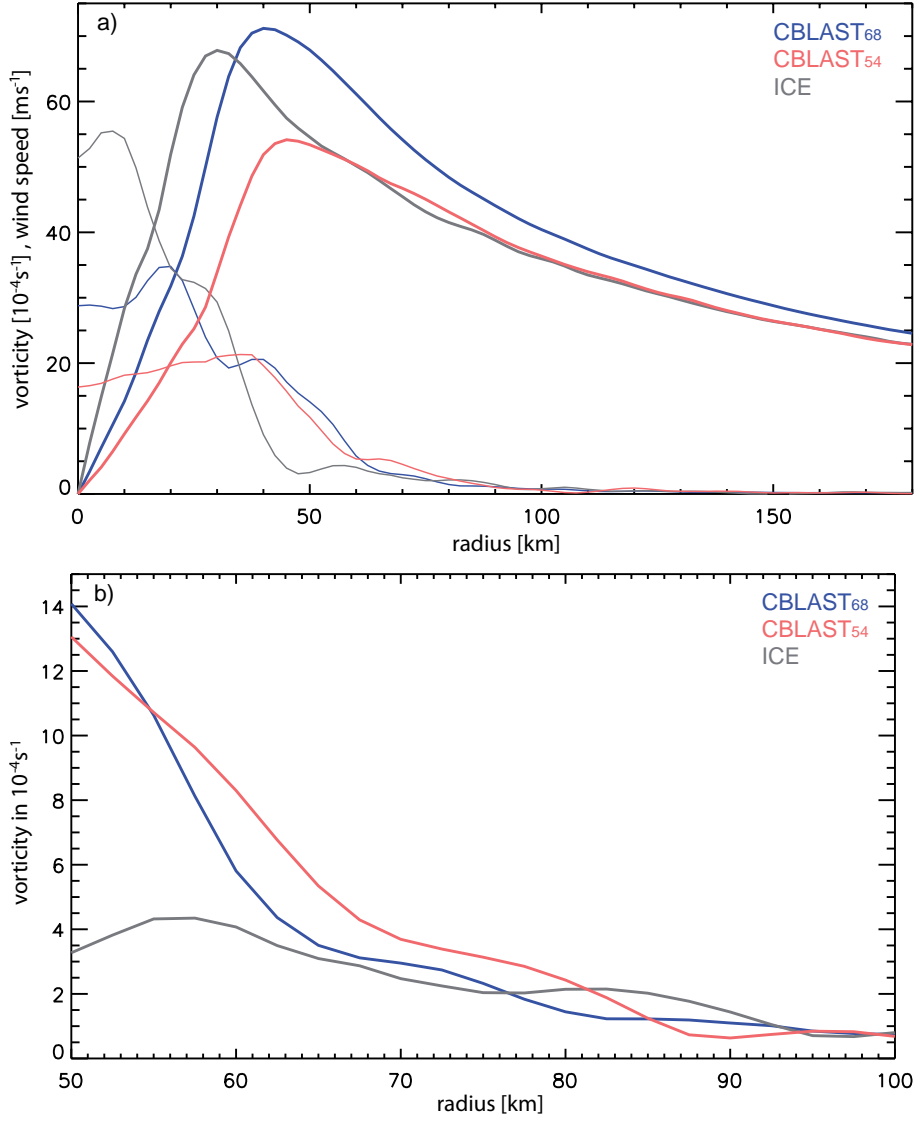
Fig. 1. (a) Radial profiles of azimuthal mean vorticity at 2 km (thin) and azimuthal mean tangential wind at the radius of maximum winds at 1 km height (thick) at the time when vertical wind shear is imposed in RMN_{54} (red), $CBLAST_{68}$ (blue), and ICE_{68} (grey), respectively. (b) Radial vorticity profiles as in (a) but zoomed in on the "skirt" region between 50 km and 100 km.
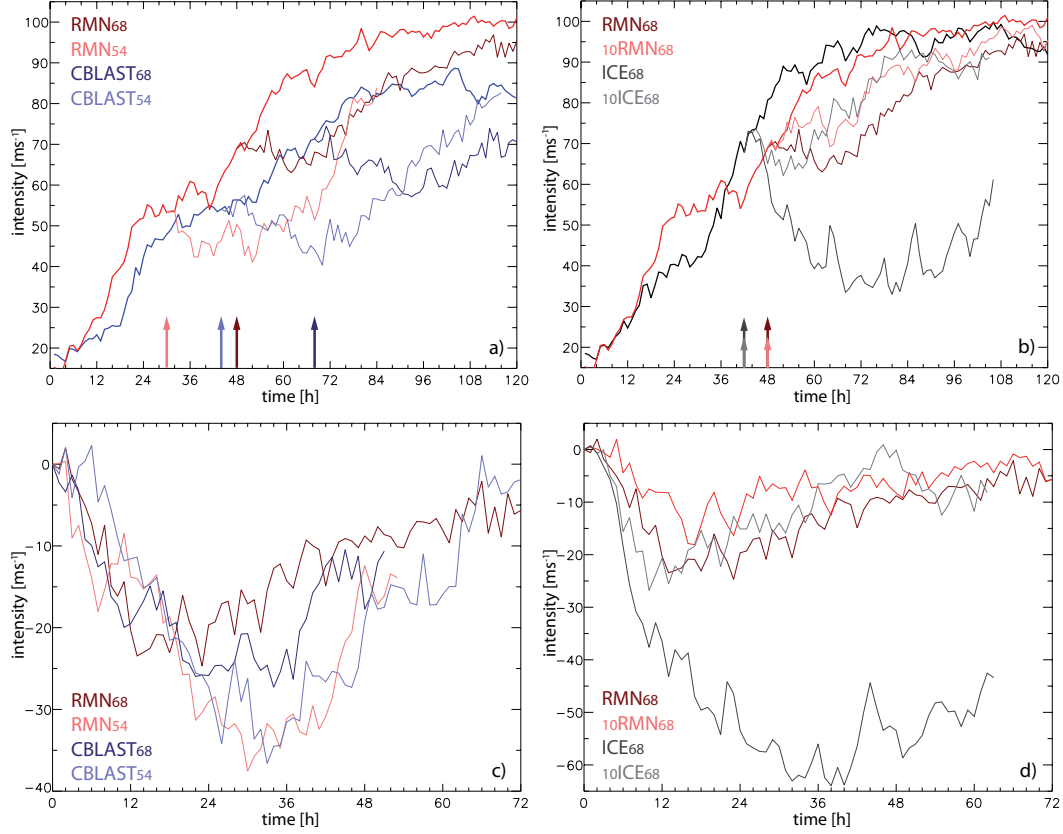
Fig. 2. a) Intensity time series for the RMN no-shear experiment (red), RMN_{54} (light red), RMN_{68} (dark red), the CBLAST no-shear experiment (blue), $CBLAST_{54}$ (light blue), and $CBLAST_{68}$ (dark blue). The colour-coded arrows denote the time when vertical wind shear is imposed in the respective experiment. b) As in a), but for the RMN no-shear experiment (red), RMN_{68} (dark red), $_{10}RMN_{68}$ (light red), the ICE no-shear experiment (black), ICE_{68} (dark grey), and $_{10}ICE_{68}$ (light grey). c) Time series of the difference between the intensity in RMN_{54} (light red), RMN_{68} (dark red), $CBLAST_{54}$ (light blue), and $CBLAST_{68}$ (dark blue) and the respective no-shear experiment. Time 0 h denotes the time when vertical wind shear is imposed in the respective experiment. d) As in c), but for RMN_{68} (dark red), $_{10}RMN_{68}$ (red), ICE_{68} (dark grey), and $_{10}ICE_{68}$ (light grey).

28
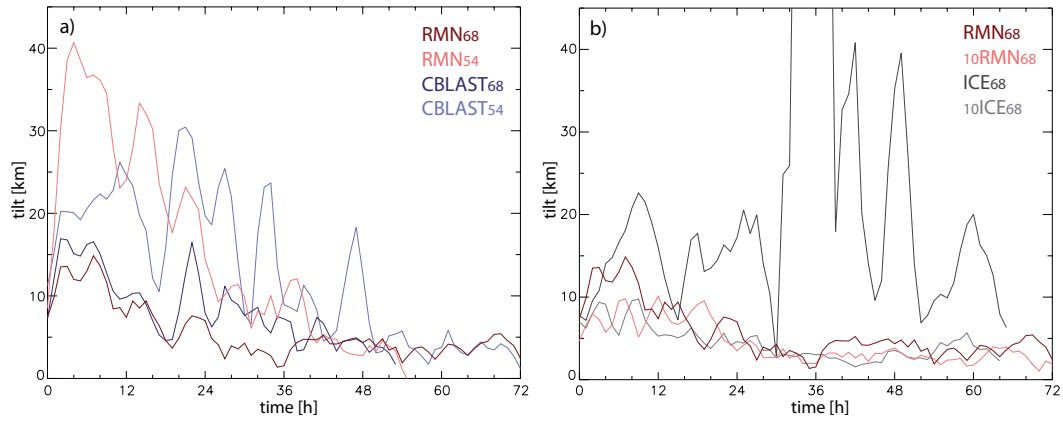
Fig. 3. a) Time series of the tilt magnitude for RMN_{54} (light red), RMN_{68} (dark red), $CBLAST_{54}$ (light blue), and $CBLAST_{68}$ (dark blue). Vortex tilt is defined as the vector difference between the vorticity centroids at 10 km and 1 km height. For visual clarity, the 3 h running mean of the time series is shown. b) As in a) but for RMN_{68} (dark red), $_{10}RMN_{68}$ (light red), ICE_{68} (dark grey), and $_{10}ICE_{68}$ (light grey). Note that the tilt magnitude for ICE_{68} goes off the scale between 33 h and 38 h reaching a maximum value of 195 km (not shown).
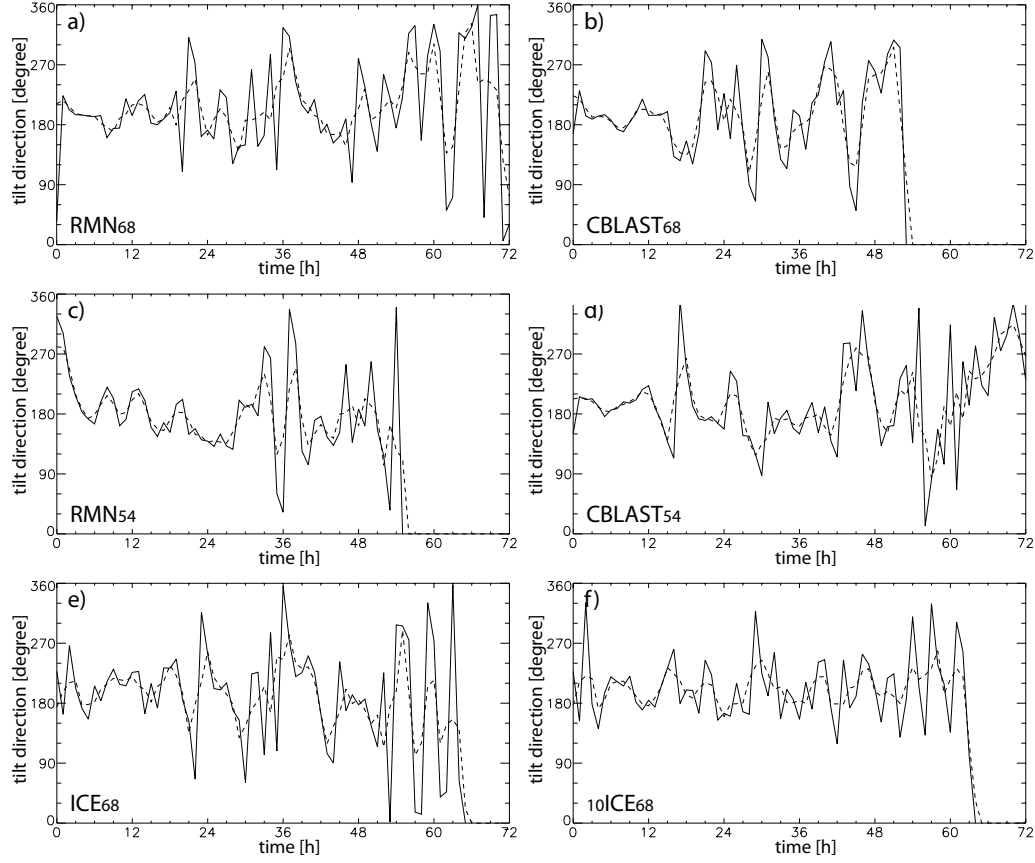
Fig. 4. Time series of the tilt direction for RMN_{68} (a), $CBLAST_{68}$ (b), RMN_{54} (c), $CBLAST_{54}$ (d), ICE_{68} (e), and $_{10}ICE_{68}$ (f). Vortex tilt is defined as the vector difference between the vorticity centroids at 10 km and 1 km height. Dashed line denotes the 3 h running mean.
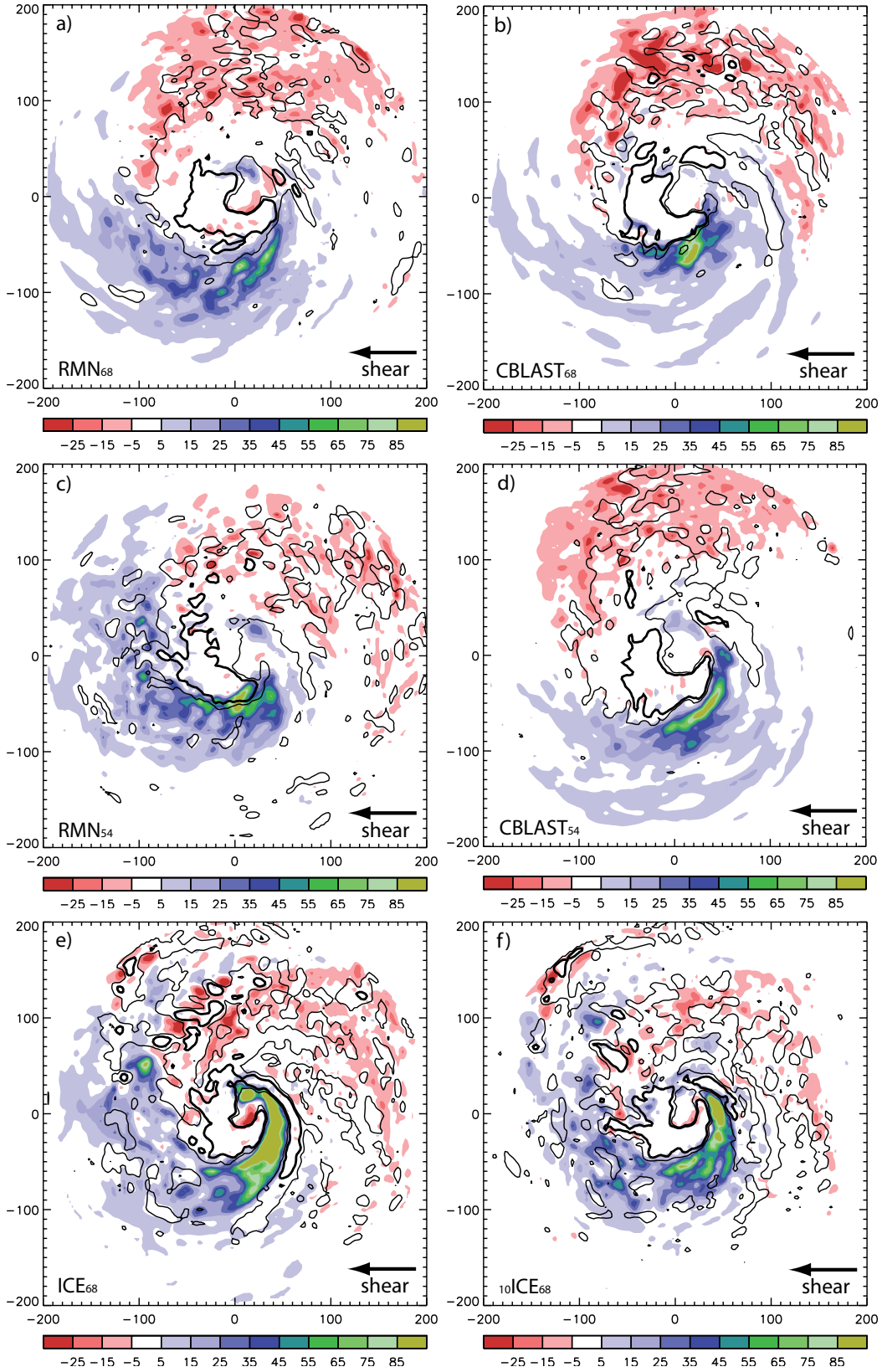
Fig. 5. Downward flux of θ'_e, DFX (colour, in 0.1 Kms^{-1}, see text for definition), at the top of the axisymmetric inflow layer, defined as 1.5 km, and low-level upward motion (thin contour: 0.25 ms^{-1}, thick contour: 1 ms^{-1}, averaged from 1.25 km - 2 km height) both averaged from 1 h - 6 h after vertical shear is imposed for a) RMN$_{68}$, b) CBLAST$_{68}$, c) RMN$_{54}$, d) CBLAST$_{54}$, e) ICE$_{68}$, and f) $_{10}$ICE$_{68}$. The arrow indicates the direction of the deep-layer shear. The horizontal scale is in km
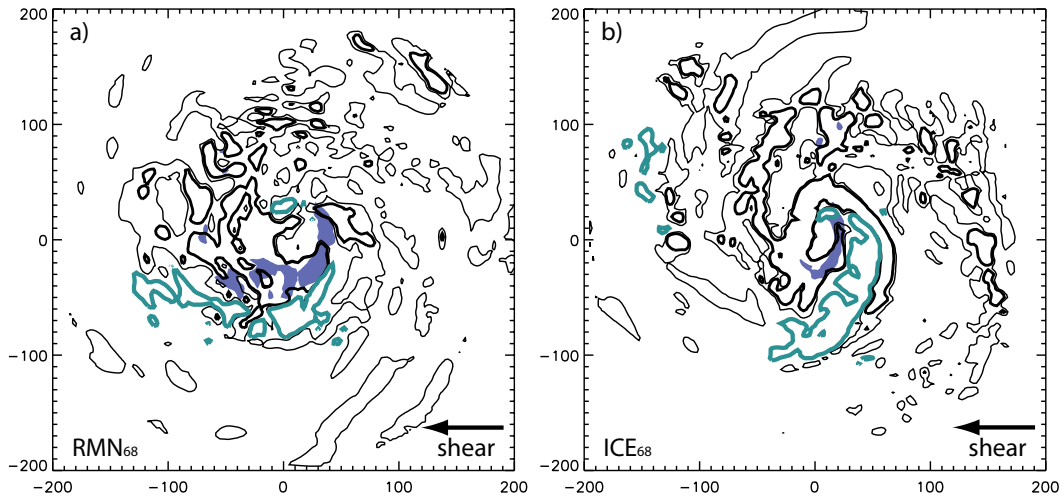
Fig. 6. Snapshots of the gradient Richardson number at 3 h after vertical shear is imposed (shaded for values below 1) in (a) RMN_{68} and (b) ICE_{68}. Upward motion is depicted in black contours (thin for 0.25 ms^{-1}, thick for 1 ms^{-1}). The cyan contour denotes regions of strong downward flux of low-θ_e air into the inflow layer (DFX at 1.5 km height, the contour depicts the 4.5 Kms^{-1} isoline). The horizontal scale is in km.
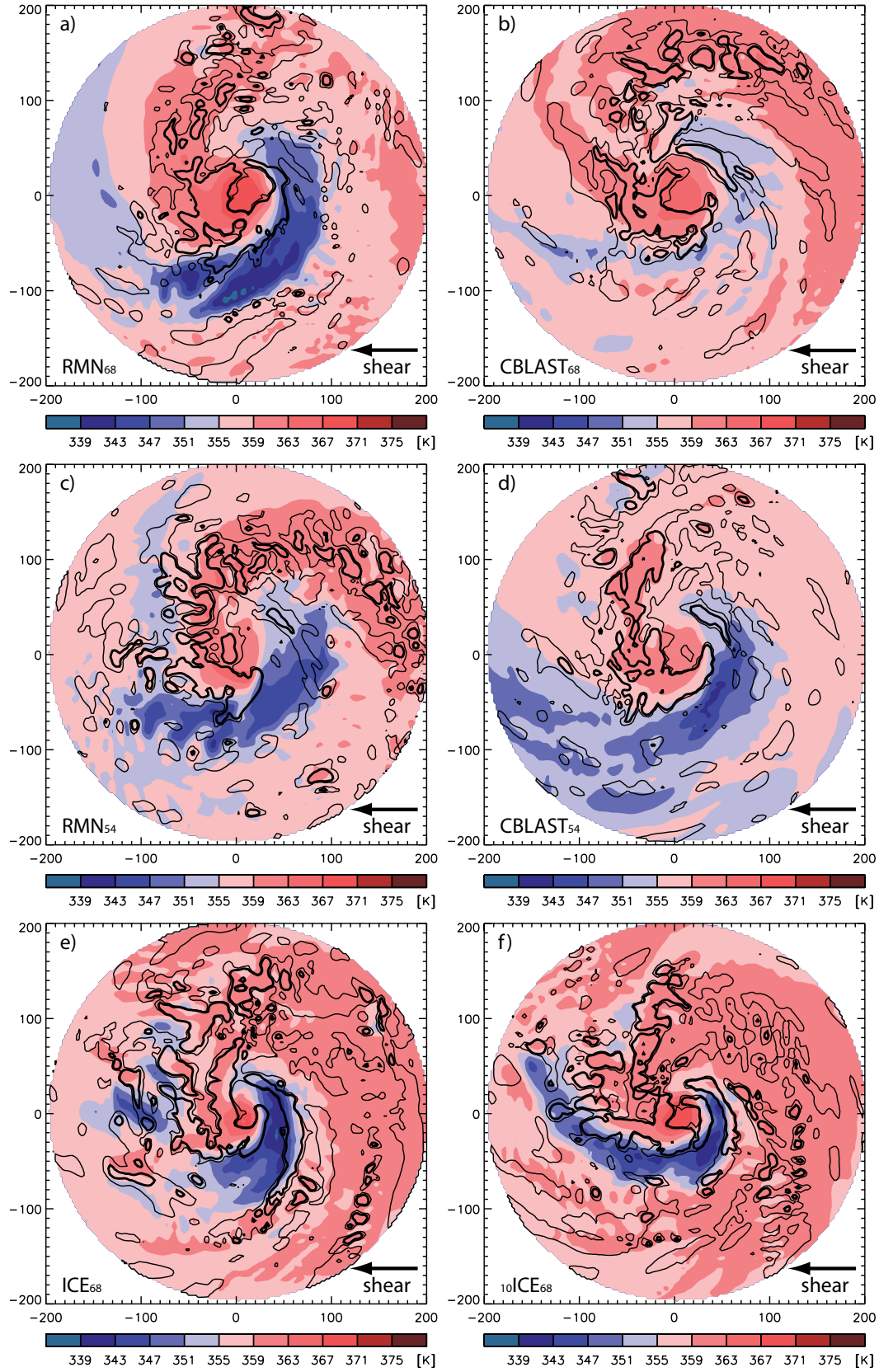
Fig. 7. As Fig. 5, but for a snapshot of inflow layer θ_e (colour, averaged over lowest 1 km) and low-level updrafts at 5 h after vertical shear is imposed for a) RMN_{68}, b) $CBLAST_{68}$, c) RMN_{54}, d) $CBLAST_{54}$, e) ICE_{68}, and f) $_{10}ICE_{68}$. The depicted time is representative for the early part of the experiments.
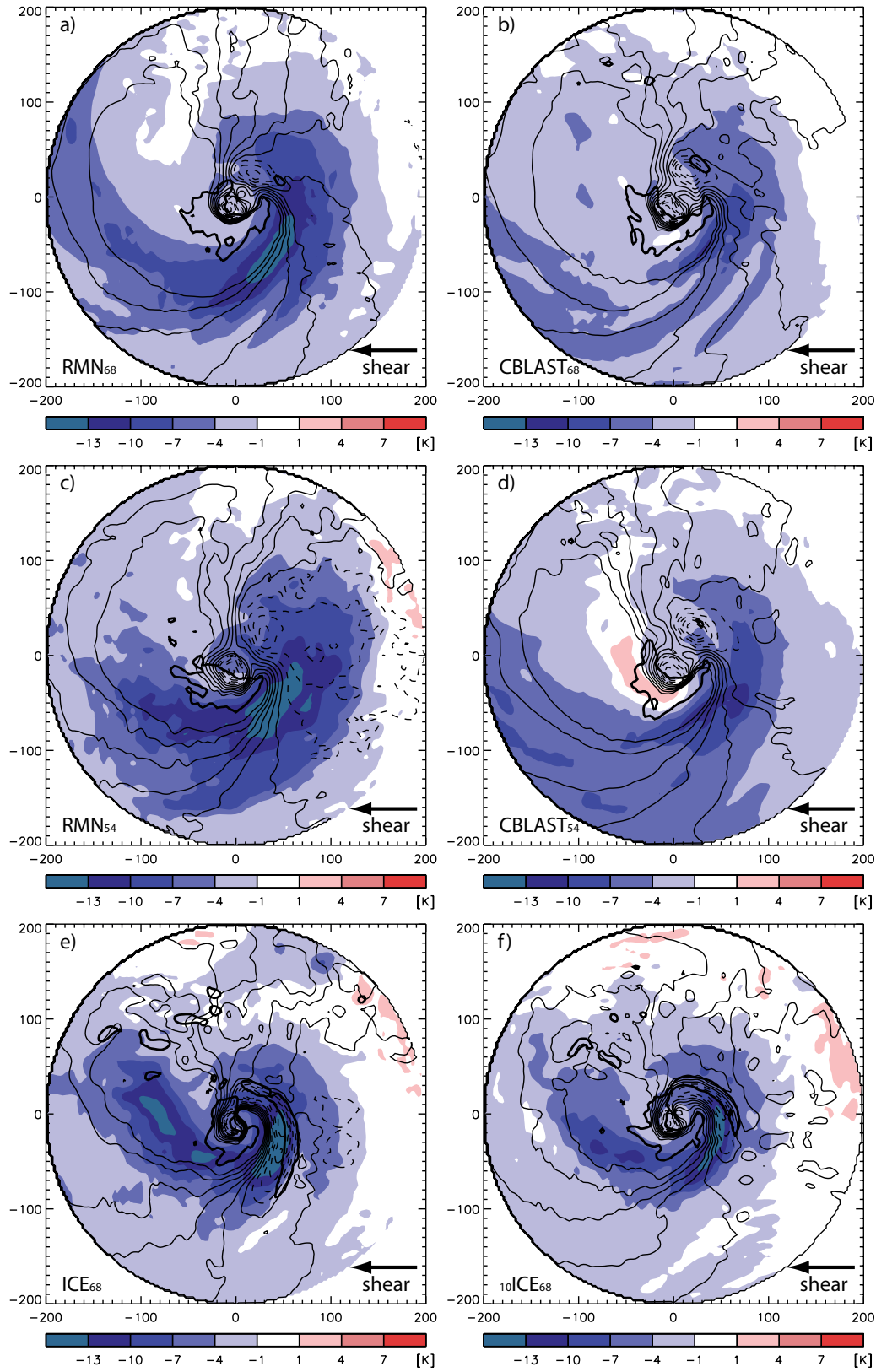
Fig. 8. Depression of inflow layer θ_e (averaged over the lowest 1 km and from 4 h - 9 h) relative to the axisymmetric mean at the time when vertical wind shear is imposed (colours). Thin contours depict the radial flow averaged over the lowest 1 km (every 4 ms^{-1}, starting at 2 ms^{-1}, dashed for negative values (outflow)). Thick contour denotes low-level updrafts (1 ms^{-1}, averaged from 1.25 km - 2 km height). a) RMN$_{68}$, b) CBLAST$_{68}$, c) RMN$_{54}$, d) CBLAST$_{54}$, e) ICE$_{68}$, and f) $_{10}$ICE$_{68}$
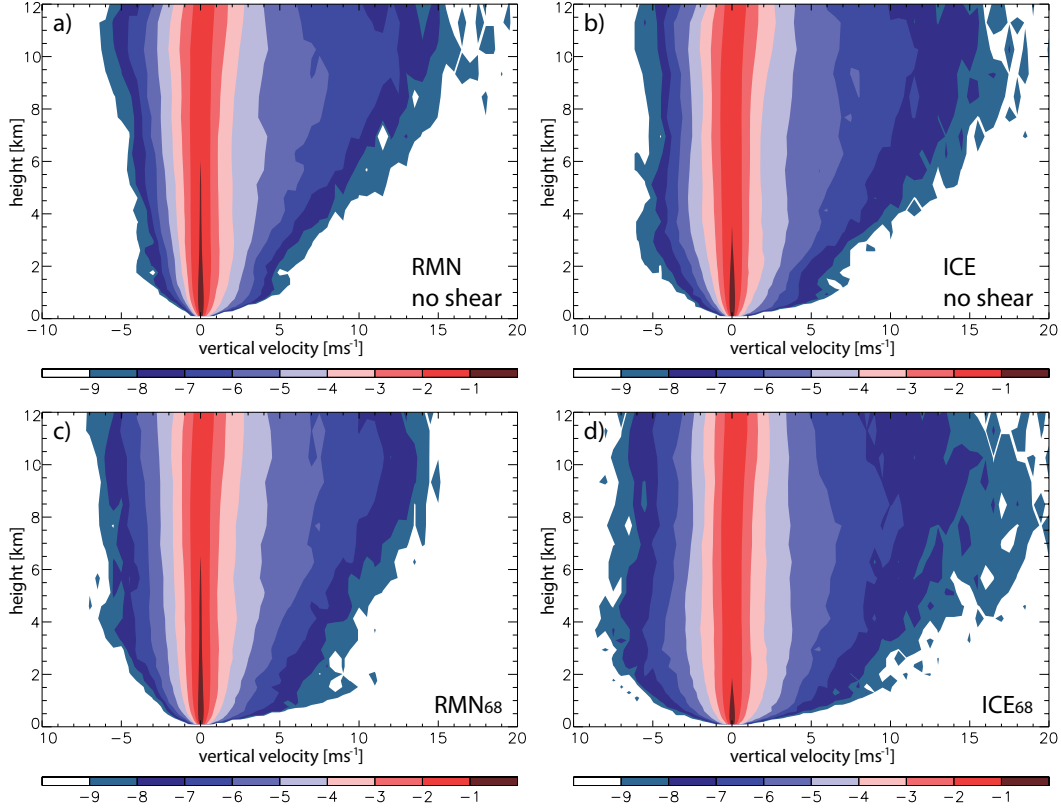
Fig. 9. Contoured frequency by altitude diagrams of vertical motion within 160 km radius of the centre. Vertical motion is binned into intervals of 0.5 ms^{-1}, centred on the values given on the x-axis. The colour-coded value denotes the logarithm of the frequency. With each contour the frequency decreases by a factor of $1/e$. Before taking the logarithm of the frequency a small positive value ($10^{-5} \approx e^{-11.5}$) has been added to ensure that the logarithm is well defined everywhere. For the no-shear cases of RMN (a) and ICE (b) the 6 h time period after vertical wind shear is imposed in the respective shear runs is considered. For RMN$_{68}$ (c) and ICE$_{68}$ (d) the times 4 h - 9 h are considered.
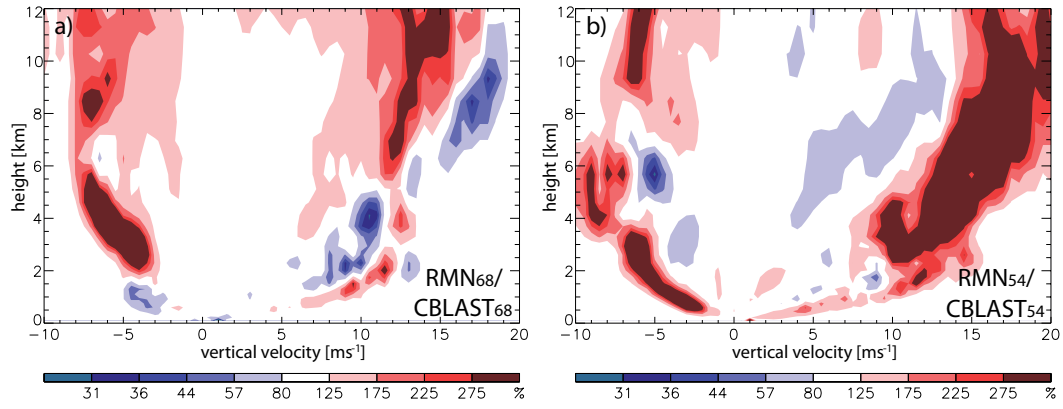
Fig. 10. As Fig. 9, but for the ratio of vertical motion frequency of $RMN_{68}/CBLAST_{68}$ (a) and $RMN_{54}/CBLAST_{54}$ (b).
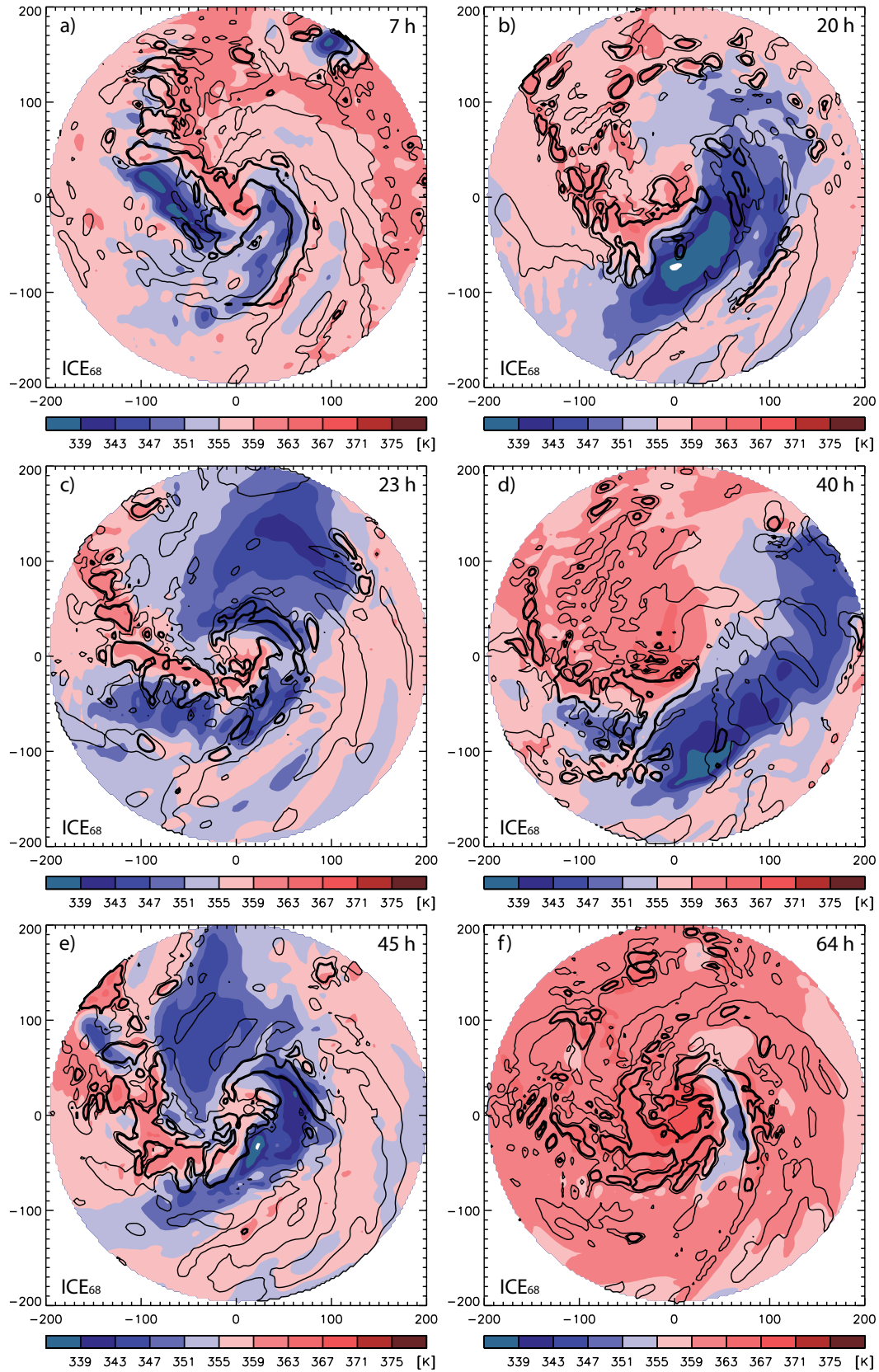
Fig. 11. As Fig. 7, but for ICE$_{68}$ at a) 7 h, b) 20 h, c) 23 h, d) 40 h, e) 45 h, and f) 64 h.